Hybrid Reconstruction Method for Indirect Monitoring of an Ice Load of a Steel Gate in a Cold Region

Meng Zhang[1], Binbin Qiu[1], Hamed Kalhori[2], Xianqiang Qu[1*]

1. Engineering Structure Lab, College of Shipbuilding Engineering, Harbin Engineering University, Harbin, 150001, China

2. School of Mechanical and Mechatronic Engineering, University of Technology Sydney, Ultimo, NSW 2007, Australia

Abstract: The steel gate of a hydraulic complex may be subjected to ice loads during freezing periods in cold regions, threatening the gate safety. The ice load on the gate is usually affected by several factors, including the ice thickness, snow cover, and changes in water level and temperature. The ice pressure distribution on the gate cannot be readily estimated by theoretical analysis or empirical formulae. Therefore, structural strain and local ice pressure data were collected over 140 days during the winter of 2016–2017 to investigate the structural deformation and local ice pressure distribution. A hybrid reconstruction method (HCM) was developed for establishing the ice pressure distribution using the monitoring data, and the effectiveness of the HCM was analysed based on several uniform load patterns and the Chebyshev polynomial functions. The ice pressure distributions on the gate were reconstructed during the entire monitoring period, considering the collected data for the lowest temperature of each day. The reconstructed ice pressure distribution, i.e., the equivalent and uniform ice pressure within every individual cell, was lower than 0.1 MPa in most parts of the gate.

Keywords： Steel gate; Structural strain monitoring; Local ice pressure monitoring; Hybrid reconstruction method (HCM); Reconstruction of ice pressure distribution;

1 Introduction

A gate is a controlling device for closing and opening the flood discharge passage, which is an important part of a hydraulic structure and is used to intercept the water, control the water level, regulate the flow, and discharge the sediment and floats. During freezing periods, especially in cold regions or high latitudes, the deformation of the steel gate may be very large due to the ice load, which may affect the normal use of the gate and even threaten its safety.

The ice load exerted on structures in cold regions can be as the result of several factors including the change in temperature, wind conditions, water flow, ice thickness, water level fluctuation, snow cover, and ice type. The ice load can be caused by each factor individually or by their combination.

Comfort et al. (2003), Stander (2006), Abdelnour (1992) and Kharik et al. (2015) believed that the ice load could be affected by thermal expansion, snow cover, water level fluctuation, and ice type. The ice load exerted on a steel gate or a dam wall is affected by different factors. Therefore, it is difficult to accurately determine the ice load with theoretical methods. However, load identification provides an effective means to estimate the ice load (Yue et al., 2000; Brown, 2007; Brown et al., 2010; Xu et al., 2010; Zhang et al., 2018).

Ice load monitoring methods can be generally divided into two categories: direct and indirect. Direct monitoring is accomplished by direct measurement of the local ice pressure using load panels and by reconstruction of the ice pressure distribution by the interpolation of the monitoring results. Indirect monitoring is based on measuring the structural response generated by the ice load, which can then be reconstructed by an appropriate inverse method.

Gong et al. (1999) described the process of a three-year programme conducted to measure ice loads on stoplogs. An 11-year investigation regarding static ice loads on dams was conducted by Comfort et al. (2004), and algorithms were developed to predict ice loads along the length of the dam based on measurements. Different types of sensors (Carter panel, BP gauge, and biaxial gauge) have been used by different research teams to measure ice loads for several years, and the ice line load obtained from different sensors agreed with each other quite well (Taras et al., 2011). Additionally, a new impact panel has been successfully used by Gagnon (2008) to measure ice pressure during the collisions of an icebreaker (CCGS Terry Fox) with bergy bits and a small iceberg.

It can be found from the abovementioned research that the ice load, including the static and dynamic load, can be measured directly by appropriate sensors when the monitored structures are suitable for their placement. However, for many applications, the placement of sensors is not readily accessible, and thus, indirect monitoring techniques are required.

The motion data of ice breakers were monitored by Johnston et al. (2008), Lee et al. (2016), and Sang et al. (2018), from which the global ice loads were determined using an inverse method. One of the recommended methods for ice load monitoring of ship structures by the American Bureau of Shipping, the shear strain difference, has been used by Ritch et al. (2008) and Jeon (2018) to calculate local ice pressure distribution according to the monitored strain data, using strain gauges installed on frames. Lee et al. (2014) attached strain gauges on the hull plate of the icebreaker ARAON to identify the local ice pressure distribution.

The ice-structure interaction is a complex process that has recently been studied using stochastic-deterministic methods. For estimating the extreme ice loads, the ACER (average conditional exceedance rate) method, developed by Chai et al. (2018), can provide a reasonable extreme prediction of the ice loads on the structure by using the ice load monitoring data. Kim et al. (2018) presented a method to evaluate the local ice pressure distribution on a structure by utilizing pressure indicating film (PIF) during the ice-structure interaction process, which is different from the conventional ice load identification. Kjerstad et al. (2018) proposed an algorithm to estimate the motions and global ice loads on hull structure, utilizing conventional measurements found on board ships coupled with additional inertial measurement units. Additionally, the icebreaker Oden was discussed as a case study, and the method developed by Kjerstad et al. (2018) showed great potential in real application. The joint input-state estimation was also used for load identification using measurements, which was verified by Maes et al. (2016) using a footbridge. Additionally, the equivalent forces have been used for structural health monitoring based on a joint input-state estimation algorithm, which was described by Lourens and Fallais (2017).

The ice pressure distribution was monitored indirectly by Zhang et al. (2018) by welding vibrating wire strain gauges on the plate of a steel gate. The basic approaches for indirect monitoring of ice load mentioned by Zhang et al. (2018) and Lee et al. (2014) are similar, and these approaches include three steps. The first step is to divide the monitored area into several individual cells, and the ice pressure within every individual cell is assumed to be equivalent and uniform. Then, an influence matrix is developed by applying a uniform pressure to each cell and obtaining the responses at the monitored locations. As a result, the mapping relations between ice loads and structural responses are established. Finally, the ice pressure distribution is calculated by the appropriate inverse framework using the collected response data. Obviously, the accuracy of the ice load identification will be greatly impacted by the accuracy of the influence matrix, size of the individual cell, and inverse methods.

The ice load was not considered when designing gates with the design code of China (2013). Therefore, icebreaking, heating, or disturbance in front of the gate to ensure the safety of the gate structure during freezing periods is recommended. These methods are safe and conservative, but not scientific, and the cost is very high. In the hydraulic complex on the Songhua River in Harbin, the forebay of the hydropower station is kept ice-free throughout the winter, except if all of the water turbines stop working. Switching off the turbines can greatly reduce the flow and may result in freezing of the water within the forebay. The internal stress of the ice layer in front of the gate can be released from the no-ice area of the forebay to some extent, which can reduce the ice load exerted on the steel gate. Therefore, there is the possibility for the steel gate to overwinter without any protection. To analyse the gate safety, taking into account the ice load, the ice pressure distribution on the gate must be known. In this study, the ice load is a general term that includes the total ice force (kN), the ice pressure (MPa), the average ice line load ($kN.m^{-1}$), i.e., the total ice force within a unit width of the gate, and the ice pressure distribution, i.e., the equivalent and uniform ice pressure within every individual cell.

The ice load on the gate has already been monitored by Zhang et al. (2018). However, a couple of limitations were found in their work. (1) The true local ice pressures on some positions were unknown. Therefore, the credibility of identification results was insufficient to some degree. (2) The area of the individual cells was too large, and the true ice pressure distribution on the gate was unknown. Logically, the smaller the area of each individual cell is, the closer the computational results are to the true distribution of the ice load. (3) The perturbation of water level was unknown. Therefore, the effect of perturbation in water level on the identification results was unknown.

To overcome the shortcomings mentioned above, the structural strain, local ice pressure, and water level of a steel gate were monitored over 140 days during the winter of 2016–2017. Additionally, the number of individual cells was increased to 36. To obtain more accurate identification results, a hybrid reconstruction method (HCM), comprising two kinds of monitoring data, three mathematical models, and three inverse methods, was developed for the reconstruction of the local ice pressure distribution on the steel gate using measurements.

2 Structural monitoring

Three kinds of sensors, including vibrating wire strain gauges, local ice pressure gauges, and water level gauges, were used in this study, as shown in Fig. 1. To ensure the accuracy of the sensors and the credibility of the monitoring data, calibration of the sensors was carried out before monitoring.

The vibrating wire strain gauge was well described by Zhang et al. (2018). The local ice pressure gauge is composed of a protective shell, induction board, data wire, vibrating wires and vibrators, and a thermistor fixed inside for temperature monitoring, as shown in Fig. 1(a). The frequency of the vibrating wire changes due to the ice load exerted on the induction board, from which the average local ice pressure can be obtained. The water level gauge is composed of a protective shell, pressure sensor, permeable stone, and data wire, as shown in Fig. 1(b).

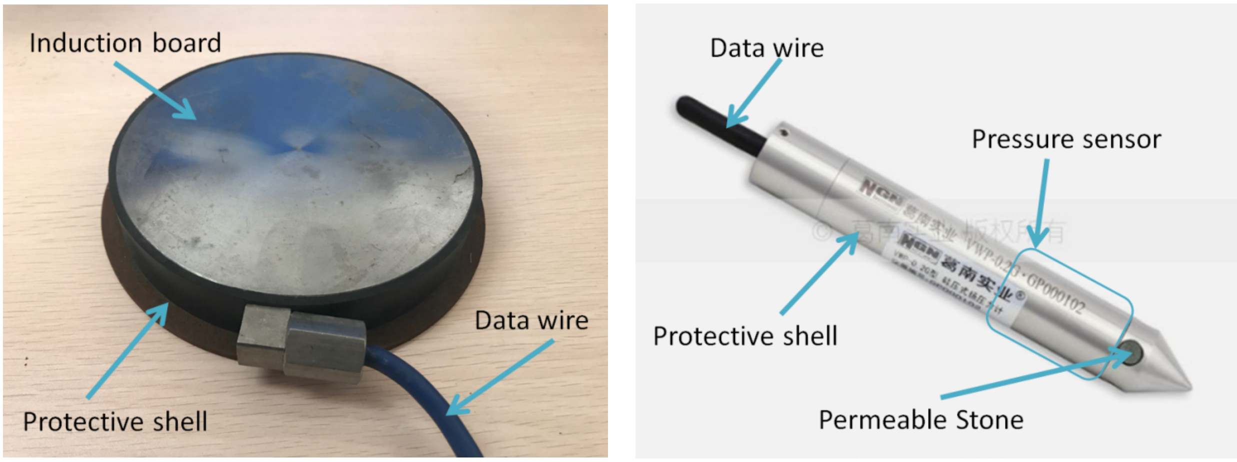

(a) (b)

Fig. 1 Monitoring gauges: (a) local ice pressure gauge and (b) water level gauge

The MCU-32 automatic data acquisition system was used to collect the monitoring data of the strain gauges, local ice pressure gauges and water level gauges every hour, and each process of data collection could be completed within 3 seconds. The specifications of the strain gauge, the local ice pressure gauge and the water level gauge are shown in Tables 1, 2 and 3, respectively. The abbreviation F. S in Tables 1–3 denotes full scale.

Table 1 The spec of the strain gauge

Size	Length		100 mm
	Effective diameter		22 mm
	End diameter		24 mm
Performance parameter	Measuring range	Tension	1500 $\mu\varepsilon$
		Compression	1500 $\mu\varepsilon$
	Accuracy of strain		±0.1% F. S
	Measuring range of temperature		-40–+150℃
	Accuracy of temperature		±0.5℃

Table 2 The spec of the local ice pressure gauge

Size	Diameter	225 mm
	Thickness	26 mm
Performance parameter	Measuring range of pressure	0–700 kPa
	Accuracy of pressure	±0.1% F. S
	Measuring range of temperature	-40–+80℃
	Accuracy of temperature	±0.5℃

Table 3 The spec of the water level gauge

Size	Length	136 mm
	Diameter	24 mm
Performance parameter	Measuring range	0–20 m
	Accuracy	≤2 mm

The Dadingzishan hydraulic complex is located in Harbin City, China, 45°59’14.75” N, 127°14’2.9” E, and 106 metres above sea level, as shown in Fig. 2. The lowest temperature of 2016–2017 was recorded at approximately −27° C.

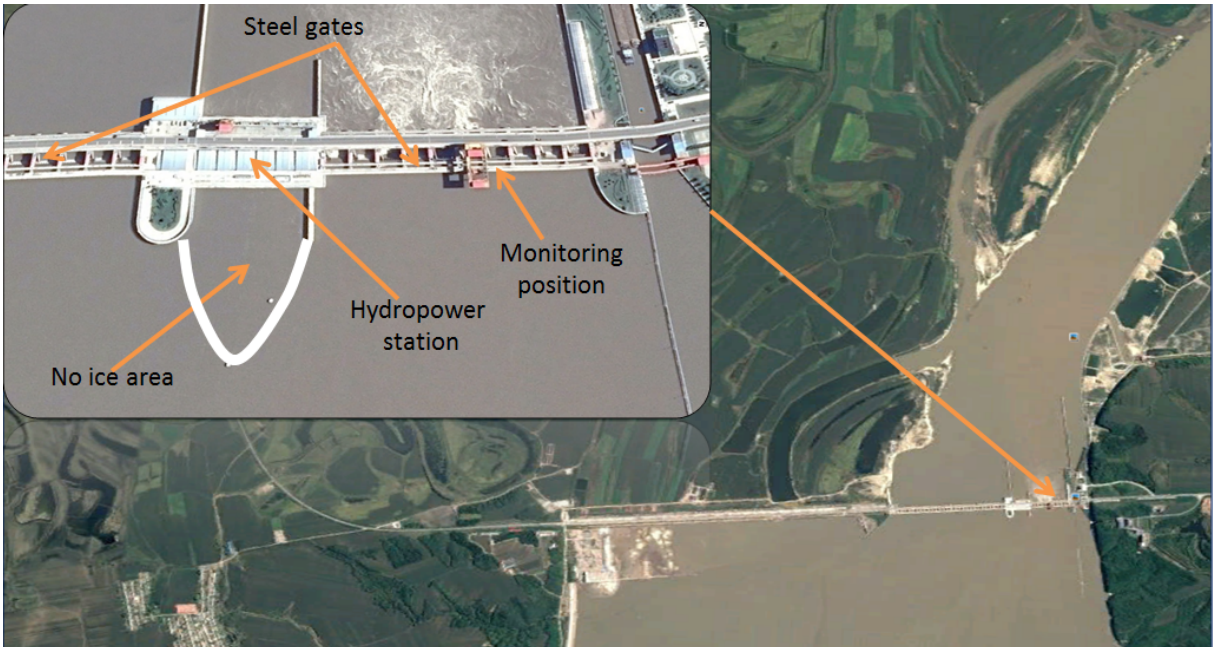

Fig. 2 Photograph of the hydraulic complex

The monitoring of the local ice pressure, structural strain, and water level was performed during the winter of 2016–2017. The ice thickness and depth of snow cover were measured approximately every 20 days during the winter. In this study, the structural strain was measured by 30 strain gauges, as shown in Figs. 3(a) and 4(a), and the local ice pressure was monitored by 6 local ice pressure gauges, as shown in Figs. 3(b) and 4(b). Two water level gauges were used to monitor the water level, which were located at the bottom of the gate.

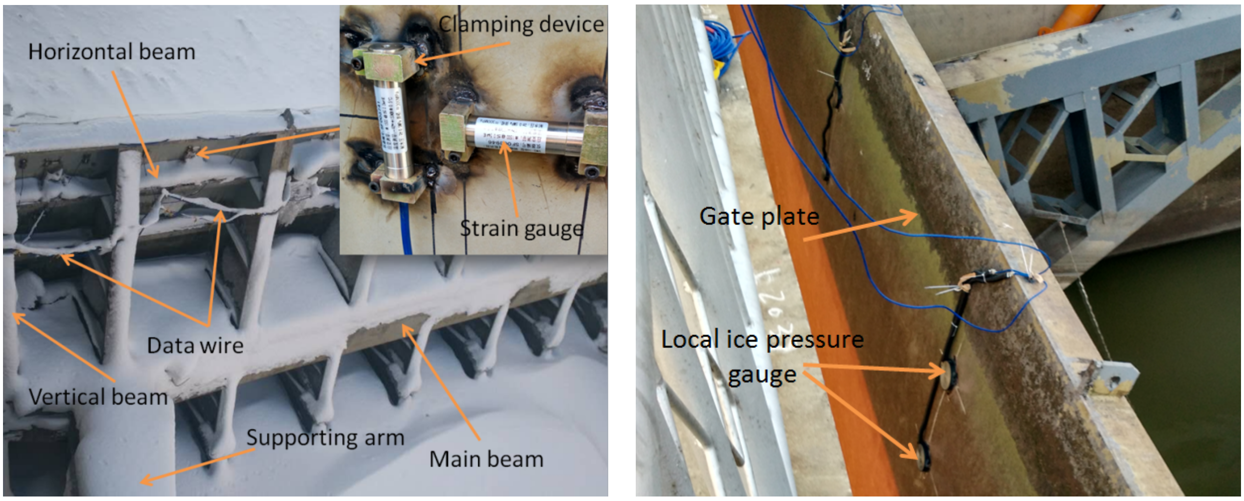

(a) (b)

Fig. 3 Installation of (a) strain gauges and (b) local ice pressure gauges

The local ice pressure gauges were welded to the surface of the gate, as shown in Fig. 3(b) and Fig. 4(b). The blue rectangle shown in Fig. 4 is the pre-estimated ice loading zone, according to the experience of the operator.

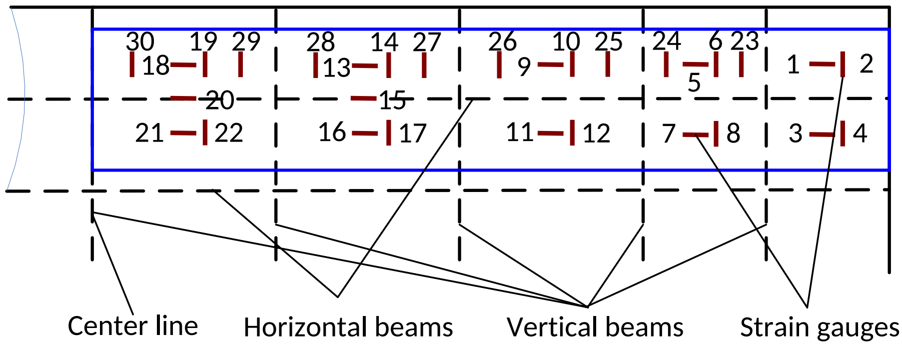

(a)

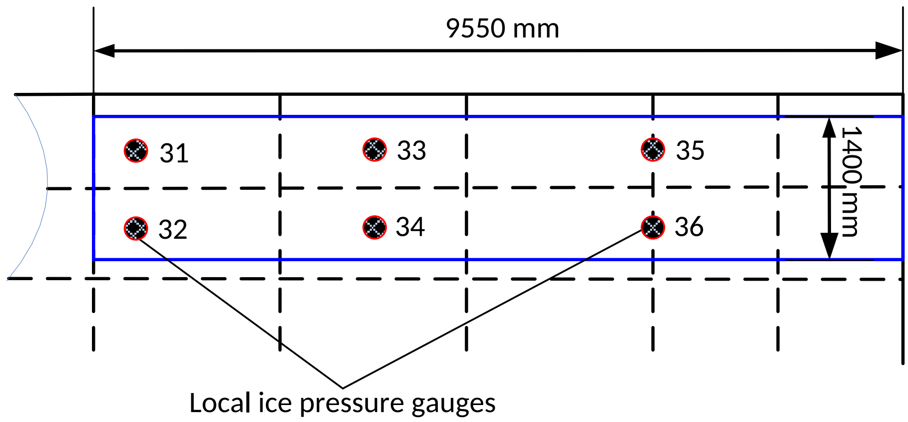

(b)

Fig. 4 Arrangement of (a) strain gauges on the back side of the gate and (b) local ice pressure gauges on the front side of the gate (in direct contact with ice/water)

3 Mathematical model for ice load reconstruction

The pre-estimated ice loading area of the steel gate was divided into 72 individual cells, which are symmetrical about the centre line, as shown in Fig. 5. The mathematical model for ice load reconstruction can be established by numerical simulation (Coates et al., 2008; Nakamura et al., 2012) and, in this study, the mathematical model is based on three assumptions:

(1) The ice load exerted on every individual cell is equivalent and uniform.

(2) The ice load exerted on the steel gate is symmetrical about the centre line of the gate.

(3) The relationship between the ice load and structural response is linear.

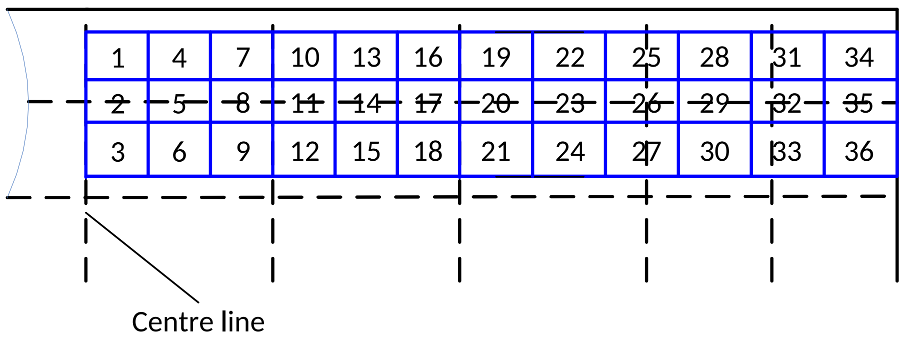

Fig. 5 Individual cells

The size of the individual cell of the ARAON icebreaker for ice load identification is approximately 0.33 m^2 (Lee et al., 2014), and the sizes of the individual cells of the CCGS icebreaker are 0.08 m^2, 0.12 m^2, and 0.24 m^2 (Ritch et al., 2008). In this study, the sizes of the individual cells are set from 0.29 m^2 to 0.45 m^2. The cells are of different sizes to ensure that the local ice pressure gauges are mounted on the centres of the cells.

The structural finite element model (FEM) was constructed using 2D shell elements (shell281). Additionally, the FEM of the steel gate was calibrated by Zhang et al. (2018), and the calibration results showed that the element size was 50 mm. Therefore, the element size of FEM in this study was set to 50 mm. The material was defined according to the gate material. The vertical displacement of the gate bottom and all the displacements of the supporting-arm endpoints were restricted, as shown in Fig. 6.

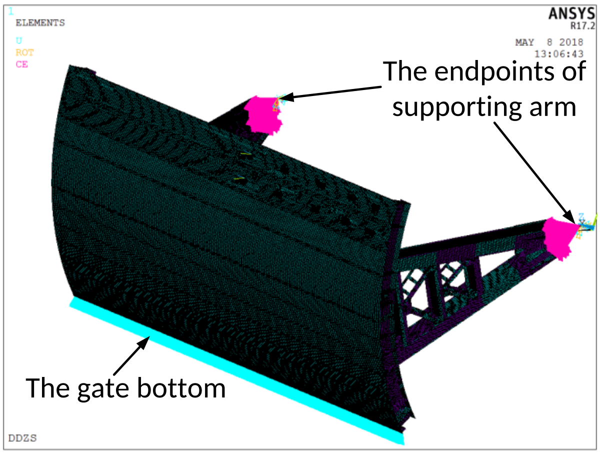

Fig. 6 FEM of the steel gate

3.1 Mathematical model 1

Mathematical model 1, which indicates a relationship between the ice pressure distribution and the monitoring data (structural response and local ice pressure), can be expressed as:

$$\begin{bmatrix} K_{11} & K_{12} & \cdots & K_{1m} \\ K_{21} & K_{22} & \cdots & K_{2m} \\ \vdots & \vdots & \ddots & \vdots \\ K_{n1} & K_{n2} & \cdots & K_{nm} \end{bmatrix}_1 \cdot \begin{Bmatrix} f_1 \\ f_2 \\ \vdots \\ f_m \end{Bmatrix} = \begin{Bmatrix} b_1 \\ b_2 \\ \vdots \\ b_n \end{Bmatrix}_1 \tag{1}$$

Eq. (1) can be expressed briefly as $[K]_1 \cdot \{f\} = \{b\}_1$, where

b_i is the measurement at location i, in which $b_1 - b_{30}$ are the structural strains ($\mu\varepsilon$) and $b_{31} - b_{36}$ are the local ice pressures (kPa),

n is the number of sensors, which is 36,

f_i is the equivalent and uniform ice pressure of cell No. i (MPa),

m is the number of cells, which is 36, and

$[K]_1$ is the transfer matrix, representing the relationship between the equivalent uniform ice pressure within different cells and the measurements obtained from the strain and local ice pressure gauges. The first 30 rows of transfer matrix $[K]_1$, i.e., the transfer matrix $[K]_2$ of mathematical model 2, were numerically obtained, and the accuracy was verified by Zhang et al. (2018) through an experiment.

The transfer matrix $[K]_1$ is established by applying a unit uniform load to a single cell and simulating the measurements at the gauge locations. This process is repeated for each cell. For example, K_{ij} indicates the strain or local ice pressure at location i due to the uniform pressure within the individual cell No. j.

In this study, the local ice pressure gauges No. 31–No. 36 were arranged on the plate within the individual cells No. 1, No. 3, No. 13, No. 15, No. 25, and No. 27, respectively, as shown in Fig. 6.

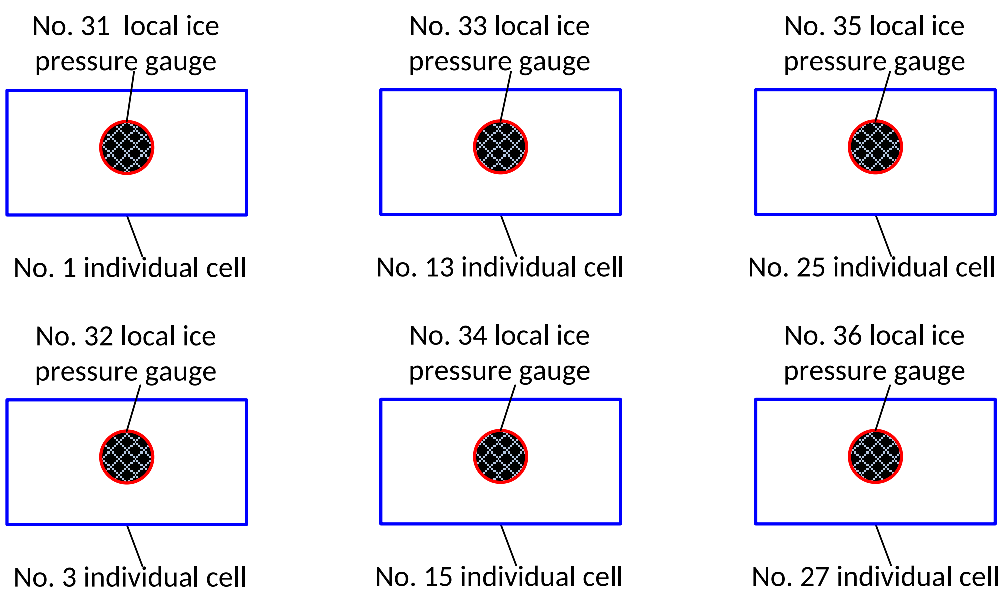

Fig. 7 Six local ice pressure gauges were arranged on six individual cells

By applying the uniform pressure of 1 MPa on cell No. 1, the structural strains at the locations of the strain gauges can be simulated using ANSYS, which then give b_1–b_{30}. Additionally, the local ice pressure gauge No. 31 was arranged on the plate within cell No. 1, the measurement of the local ice pressure gauge No. 31 was set to 1000 kPa, and the measurements of the other local ice pressure gauges were set to 0 kPa when applying the uniform pressure of 1 MPa only on cell No. 1. It should be noted that, in this study, the unit of the local ice pressure gauge is kPa, and the unit of the identified ice pressure within every cell is MPa.

The transfer matrix $[K]_1$ contains two kinds of elements: structural strain and local ice pressure. Once the complete transfer matrix $[K]_1$ and the mathematical model 1 were obtained, the reconstruction of the local ice pressure distribution becomes a problem of solving an ill-posed linear system of equations with the condition number of the transfer matrix $[K]_1$ equal to 2217. Solving the mathematical model $[K]_1 \cdot \{f\} = \{b\}_1$ is equivalent to finding 36 unknowns by 36 known quantities. Additionally, the transfer matrix can also be established using step relaxation functions as described by Ewins (2000) and evaluated at 0 Hz frequency.

The conventional ice load identification comprises three main steps:

(1) constructing a mathematical model that indicates the relationship between the structural response and the applied ice load,

(2) monitoring the structural response, and

(3) calculating the ice load by an appropriate inverse method using structural response monitoring data.

It can be found that mathematical model 1 is not the conventional ice load identification, in which the measured local ice pressure and structural strain are included.

3.2 Mathematical model 2

When the structural strain of $[K]_1$ and $\{b\}_1$ are taken separately, i.e., ignoring the local ice pressure of $[K]_1$ and $\{b\}_1$, another mathematical model can be obtained, and it is expressed as Eq. (2).

$$[K]_2 \cdot \{f\} = \{b\}_2 \tag{2}$$

where

$$\{b\}_2 = \begin{Bmatrix} b_1 \\ b_2 \\ \vdots \\ b_{30} \end{Bmatrix}_2 = \begin{Bmatrix} \varepsilon_1 \\ \varepsilon_2 \\ \vdots \\ \varepsilon_{30} \end{Bmatrix}_2 \tag{3}$$

In Eq. (2), the reconstruction of the ice pressure distribution becomes a problem of conventional load identification, and the condition number of $[K]_2$ is 194. Solving the mathematical model 2 is equivalent to finding 36 unknowns by 30 known quantities.

3.3 Mathematical model 3

In this study, the ice load on the steel gate is equivalent to the uniform ice pressure within every individual cell. The mathematical models 1 and 2 mentioned above have their shortcomings. In mathematical model 1, the contact area of the local ice pressure gauge is approximately 0.04 m^2 (as shown in Fig. 1(a)), and the areas of the individual cells range from 0.29 m^2 to 0.45 m^2. The actual ice pressure within every cell is unlikely to be uniform. Therefore, the collected local ice pressure cannot be used as the equivalent uniform ice pressure of the cell. In mathematical model 2, 36 unknowns are solved through 30 known quantities, which is an under-determined problem.

In mathematical model 1, although the measured local ice pressure p cannot be used directly as the equivalent uniform ice pressure f within the cell, a relationship between them can be defined as

$$(1-\alpha)\frac{p}{1000} \le f \le (1+\alpha)\frac{p}{1000} \tag{4}$$

where

α is a constraint parameter,

p is the actual pressure (kPa) measured by the local ice pressure gauge, and

f is the equivalent and uniform ice pressure (MPa) on a cell on which the local ice pressure gauge is attached.

Finally, mathematical model 3 for reconstruction of the ice pressure distribution is defined as follows:

$$\begin{cases} \left[K\right]_2 \cdot \{f\} = \{b\}_2 \\ \text{Constraints:} \\ (1-\alpha)p_{31}/1000 \le f_1 \le (1+\alpha)p_{31}/1000 \\ (1-\alpha)p_{32}/1000 \le f_3 \le (1+\alpha)p_{32}/1000 \\ (1-\alpha)p_{33}/1000 \le f_{13} \le (1+\alpha)p_{33}/1000 \\ (1-\alpha)p_{34}/1000 \le f_{15} \le (1+\alpha)p_{34}/1000 \\ (1-\alpha)p_{35}/1000 \le f_{25} \le (1+\alpha)p_{35}/1000 \\ (1-\alpha)p_{36}/1000 \le f_{27} \le (1+\alpha)p_{36}/1000 \end{cases} \tag{5}$$

In this section, three mathematical models were constructed, which were used for ice-load reconstruction. Models 1 and 2 are linear systems of equations, which can be solved directly by implementing conventional regularisation methods, including the Tikhnov regularisation method (TRM) and the truncated singular value decomposition (TSVD), in which the regularisation parameter can be defined through the L-curve method (L-curve) or generalized cross validation (GCV) (Wang et al., 2015; Kalhori et al., 2016; Hansen, 2007).

Model 3 is a linear system of equations with constraints, which can be solved using many methods, such as particle swarm optimization method (PSO) and the genetic algorithm (GA) (Chuang et al., 2016), etc. In this study, the GA was used to solve the linear system of equations with constraints, i.e., the model 3. There are some advantages for the GA in obtaining optimal solutions, which are: (1) an objective function can be defined and used to search optimal solutions within a defined range, and the whole programme is easy to define; (2) a probabilistic mechanism is introduced in the iterative computation process, resulting in randomness of the results, which is beneficial to obtain better solutions; and (3) the GA algorithm has good expansibility and is easy to combine with other algorithms. However, the solving speed of a GA may be too low, and the GA may fall into the local optimal solution, resulting in poor accuracy, which are the shortcomings of the GA.

4 Hybrid reconstruction method

A hybrid reconstruction method (HCM) was developed for the reconstruction of ice pressure distribution based on the GA, in which the conventional regularisation solutions of models 1 and 2 were used as the initial solutions of the GA for solving model 3, which can accelerate the solving process of the GA for model 3 and is beneficial for obtaining global optimal solution.

In the application of GA, a problem first is defined as objective functions and constraints. Then, initial solutions are generated randomly, which is a conventional method for generating initial solutions. The number of initial solutions is usually from tens to hundreds. Then, the optimal solution is searched using the operations of selection, crossover and mutation, in which the initial solutions are the beginning of searching optimal solution. Therefore, the HCM maintains the advantages and overcomes the disadvantages of GA to some extent.

4.1 Conventional regularisation methods for mathematical model 1

To analyse the accuracy of the regularisation methods, an actual situation was considered, where the structural strain and local ice pressure data collected by the strain and local ice pressure gauges, respectively, contained a certain amount of errors. The simulation steps are as follows:

Step 1: Four kinds of ice pressure distribution $\{f\} \in \mathbb{R}^{36\times1}$, such as the 'Original' shown in Fig. 8, are employed based on the assumption that the ice pressure is equivalent and uniform within each individual cell. Additionally, most elements of $\{f\} \in \mathbb{R}^{36\times1}$ are non-zero.

Step 2: Application of ice pressure distribution $\{f\} \in \mathbb{R}^{36\times1}$ to the FEM of the gate. The structural strains at the 30 structural strain monitoring locations are calculated. Then, the local ice pressures at the 6 local ice pressure monitoring locations, i.e., the $p_{31} - p_{36}$, are set to the ice pressures exerted on the 6 individual cells, i.e., No. 1, No. 3, No. 13, No. 15, No. 25 and No. 27 individual cells, on which the local ice pressure gauges are arranged, as shown in Fig. 7. For example, the No. 31 local ice pressure gauge is arranged on the No. 1 individual cell, the pressure exerted on the No. 1 individual cell is used as the monitoring pressure data of No. 31 local ice pressure gauge, i.e., p_{31}. Finally, the simulated monitoring data $\{b\}_1 \in \mathbb{R}^{36\times1}$ is obtained.

Step 3: Addition of error $\{b\}_1' = \{b\}_1 + \Delta\{b\}_1$; for the strain gauges used in the field test, the test error was set as random data from −10 to 10 $\mu\varepsilon$; for the local ice pressure gauges, the test error was set as random data from −3 to 3 kPa;

Step 4: The ice pressure distribution $\{f\}' \in \mathbb{R}^{36\times1}$ is calculated with the input of $\{b\}_1' \in \mathbb{R}^{36\times1}$ as obtained in Step 3.

The simulation results are shown in Fig. 8.

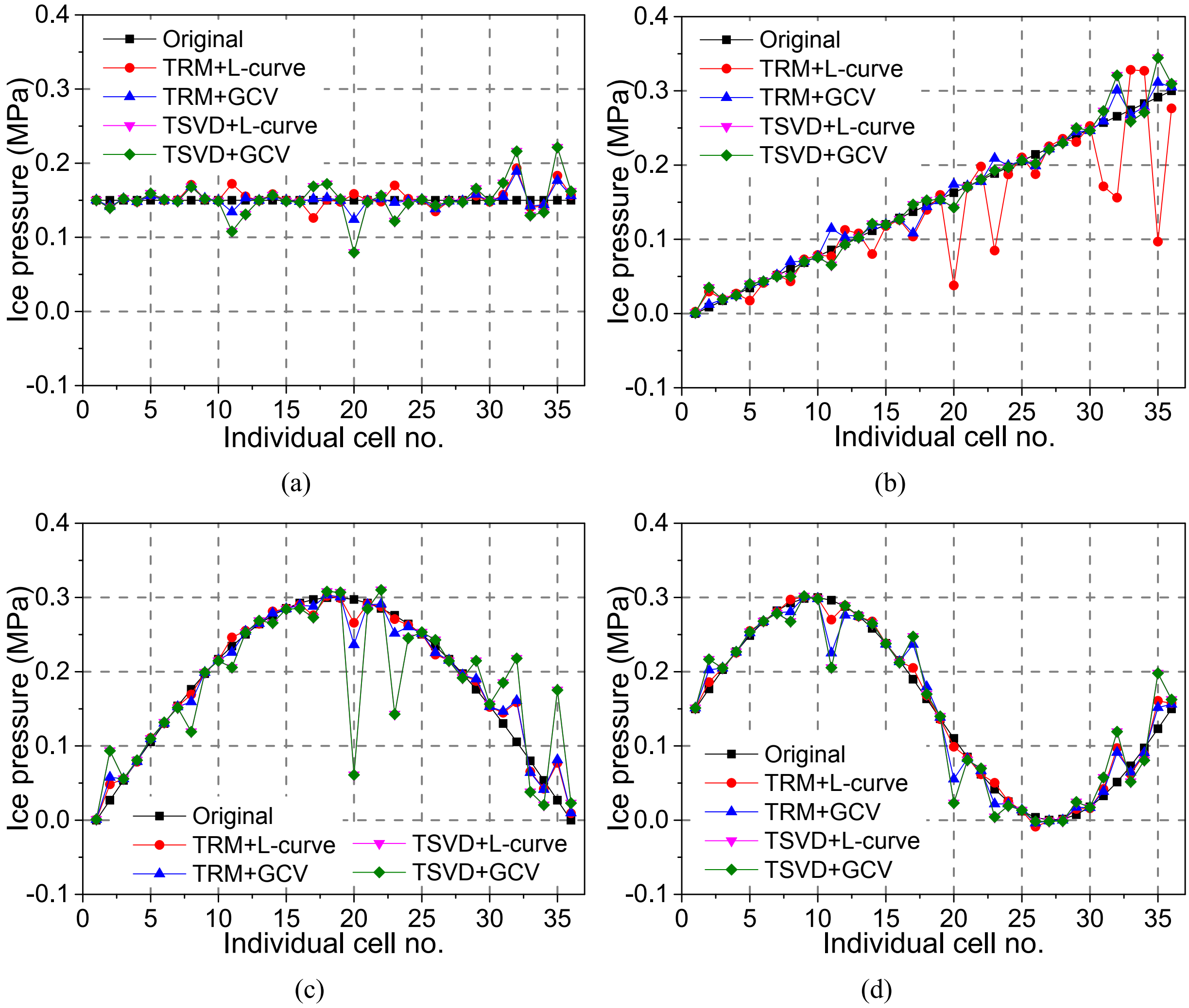

Fig. 8 Simulation results for (a) uniform load, (b) linear load, (c) quadratic load, and (d) cubic load using structural strain and local ice pressure data

Fig. 8 shows that no inverse method can produce a perfect fitting for each load pattern.

4.2 Conventional regularisation methods for mathematical model 2

Mathematical model 2 can also be solved directly by the conventional regularisation method, including the TRM+L-curve, TRM+GCV, TSVD+L-curve, and TSVD+GCV. The steps for verifying the accuracy of the conventional regularisation methods are the same as those for mathematical model 1. The simulation results are shown in Fig. 9.

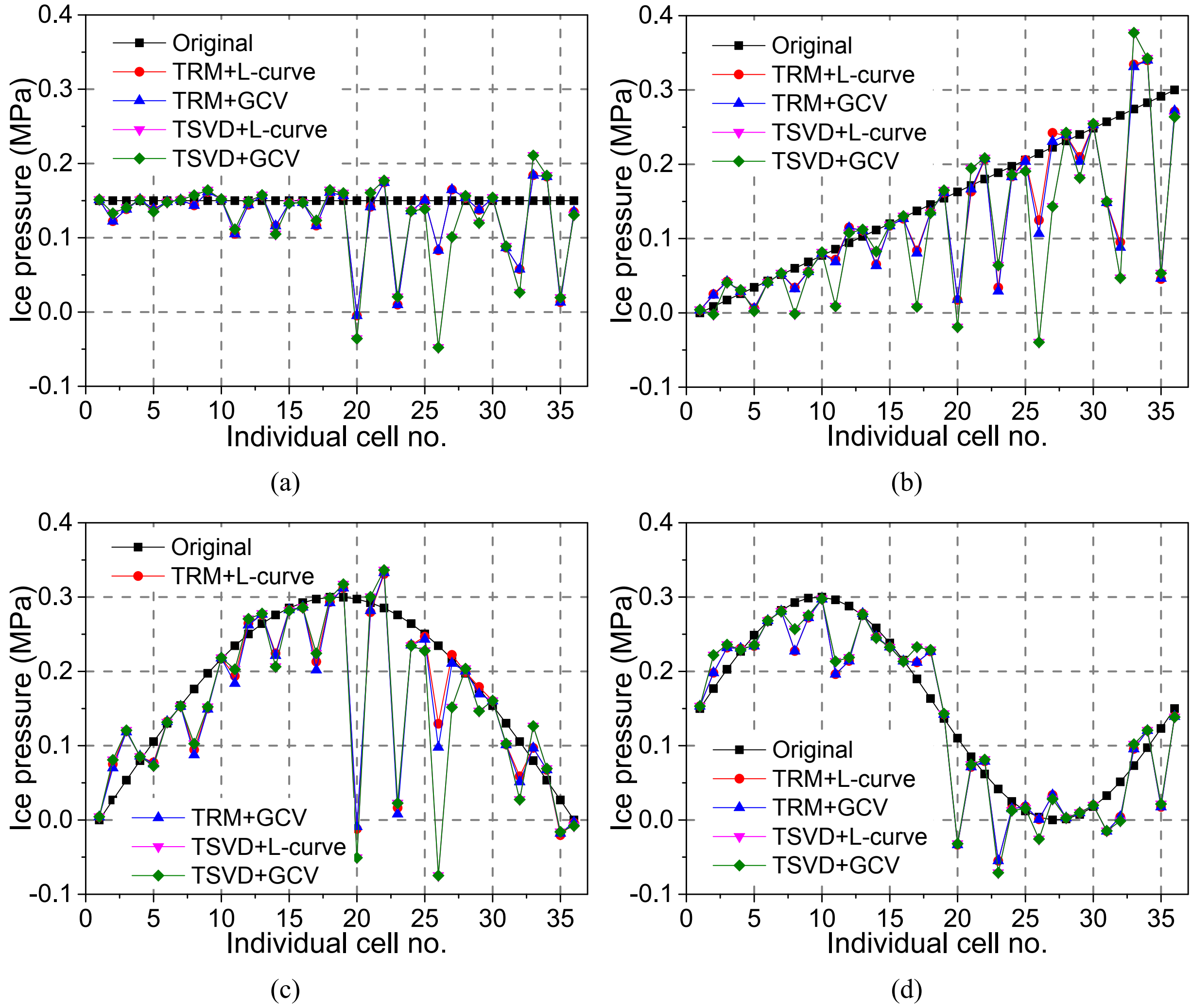

Fig. 9 Simulation results for (a) uniform load, (b) linear load, (c) quadratic load, and (d) cubic load using only the structural strain data

It can be found from Fig. 9 that no method can provide an accurate fitting, which may be due to a lack of known quantities. However, the solutions provided by the four inverse methods can be satisfactory for several individual cells, such as cells No. 1, No. 4, No. 6, No. 7, No. 10, No. 12, No. 13, No. 15, No. 16, No. 18, No. 19, No. 21, No. 24, No. 25, No. 27, No. 28, No. 30, and No. 36.

4.3 Hybrid reconstruction method for mathematical model 3

The conventional regularisation methods cannot produce a good fitting for mathematical models 1 and 2, and mathematical model 1 has its shortcomings. Additionally, because of the difference in regularisation parameters obtained from the L-curve and GCV, the solutions provided by the Tikhonov regularisation method (TRM+L-curve and TRM+GCV) are different. Similarly, the solutions provided by TSVD+L-curve and TSVD+GCV are also different.

Figs. 8 and 9 show that the solutions derived from TRM and TSVD for mathematical models 1 and 2 are accurate only within certain cells. Therefore, the HCM was developed in this study for solving mathematical model 3 (a linear system of equations with constraints).

The kernel of the HCM, as shown in Fig. 10, uses the conventional regularised solutions of mathematical models 1 and 2 as the initial solutions of the GA in mathematical model 3 to accelerate the solving process and further improve the precision of the reconstruction results. In solving mathematical models 1 and 2 using the TRM and TSVD, the regularisation parameters were directly determined covering a large scope. For example, model 1 is solved with TRM, in which the regularisation parameter is set to 0, 20,..., 960, and 980, respectively, and then a large number of initial solutions can be obtained. Those initial solutions are much better than the initial solutions generated randomly. Thus, the HCM is composed of two kinds of monitoring data (strain and local ice pressure), three mathematical models (mathematical models 1, 2, and 3), and three inverse methods (TRM, TSVD, and GA).

The specific steps of HCM are as follows:

Step 1: Mathematical model 1 is solved with the TSVD, in which the regularisation parameter is set to 16, 27, …, 34, and 35, and then 20 initial solutions can be obtained.

Step 2: Model 1 is also solved with the TRM, the regularisation parameter is set to 0, 20, …, 960, and 980, and then 50 initial solutions can be obtained.

Step 3: Mathematical model 2 is solved by the TSVD, the regularisation parameter is set to 10, 11, …, 28, and 29, and then 20 initial solutions can be obtained.

Step 4: Model 2 is also solved by the TRM, the regularisation parameter is set to 0, 20, …, 960, and 980, and then 50 initial solutions can be obtained.

Step 5: From steps 1–4, 140 initial solutions are obtained. Then, another 160 initial solutions were generated randomly.

Therefore, 300 initial solutions can be used as the initial population of the GA for mathematical model 3. The objective function is defined as:

$$L = \left\| [K]_2 \cdot \{f\} - \{b\}_2 \right\|^2 \tag{6}$$

Additionally, the following constraints must be met, and the constraint parameter α is set to 0.3.

$$\begin{cases} 0 \le f_1 \le 0.35 \\ \quad \vdots \\ 0 \le f_i \le 0.35 \\ \quad \vdots \\ 0 \le f_{36} \le 0.35 \end{cases} \tag{7}$$

$$\begin{cases} 0.7p_{31}/1000 \le f_1 \le 1.3p_{31}/1000 \\ 0.7p_{32}/1000 \le f_3 \le 1.3p_{32}/1000 \\ 0.7p_{33}/1000 \le f_{13} \le 1.3p_{33}/1000 \\ 0.7p_{34}/1000 \le f_{15} \le 1.3p_{34}/1000 \\ 0.7p_{35}/1000 \le f_{25} \le 1.3p_{35}/1000 \\ 0.7p_{36}/1000 \le f_{27} \le 1.3p_{36}/1000 \end{cases} \tag{8}$$

Eq. (7) and Eq. (8) indicate that the ice pressure within each individual cell was limited between 0 and 0.35 MPa, according to the experience of the field manager, in which the equivalent uniform ice pressures within the individual cells No. 1, No. 3, No. 13, No. 15, No. 25, and No. 27 were further restricted based on the monitoring data of the local ice pressure gauges. The HCM flowchart is shown in Fig. 10.

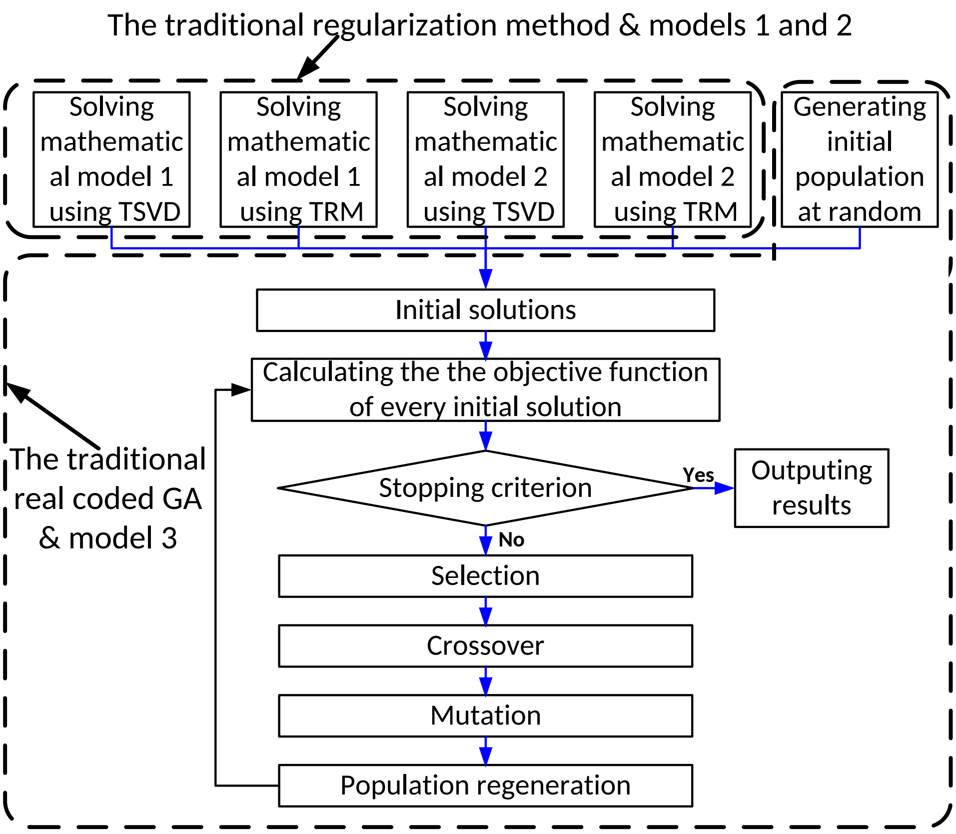

Fig. 10 HCM flowchart

The real coded GA (Tutkun, 2009; Deep et al., 2009; Tsoulos, 2008; Badran et al., 2009) and proportional selection were used in the HCM, in which the probabilities of selection, crossover, and mutation are set to 0.9, 0.8, and 0.05, respectively, and the iteration was stopped when the number of iterations reached 100. The four steps for verifying the accuracy of the HCM are the same as those in mathematical model 1. Fig. 11 illustrates the simulation results.

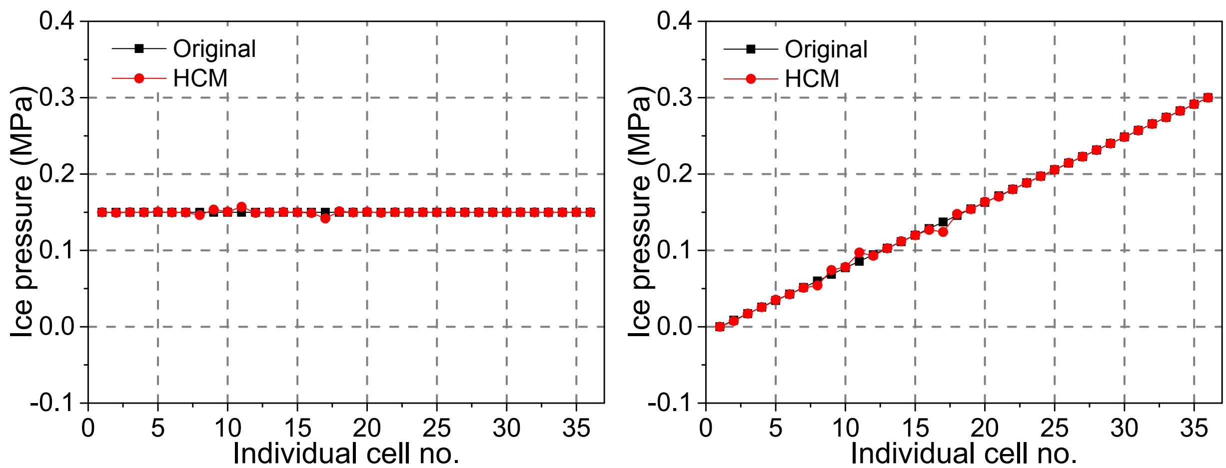

(a) (b)

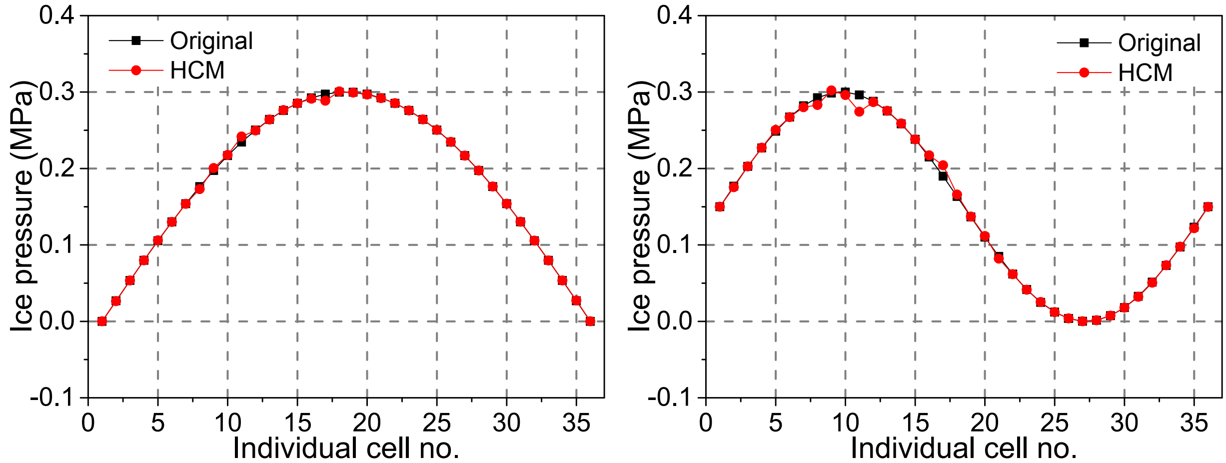

(c) (d)

Fig. 11 Simulation results with the HCM for (a) uniform load, (b) linear load, (c) quadratic load, and (d) cubic load using structural strain and local ice pressure

The simulation results in Figs. 8, 9, and 11 show that the HCM produces the most accurate solutions.

As the actual ice pressure on the gate is unlikely to be uniform within every individual cell, six load functions across the loading area of the gate were constructed to verify the effectiveness of the assumption that the ice pressure is equivalent and uniform within every cell. The simulation steps are designed as follows:

Step 1: Six load functions $f_1(x,y)-f_6(x,y)$ are assumed based on the Chebyshev orthogonal polynomials. The function-type loads are symmetrical about the centre line of the gate, and the loading area is shown in Fig. 12.

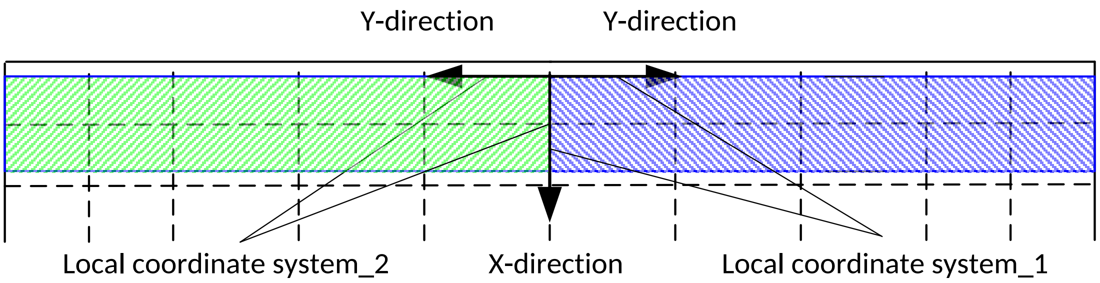

Fig. 12 Loading areas of function-type loads

The load functions are shown in Eqs. (9)–(14).

$$f_1(x,y)=\frac{0.2}{\pi}\left[2.(\frac{2}{1400}x-1)^2-1\right].\left[8.(\frac{2}{9550}y-1)^4-8.(\frac{2}{9550}y-1)^2+1\right]+0.1 \qquad (9)$$

$$f_2(x,y)=\frac{0.2}{\pi}\left[2.(\frac{2}{1400}x-1)^2-1\right].\left[16.(\frac{2}{9550}y-1)^5-20.(\frac{2}{9550}y-1)^3+5.(\frac{2}{9550}y-1)\right]+0.1 \quad (10)$$

$$f_3(x,y)=\frac{0.2}{\pi}\left[2.(\frac{2}{1400}x-1)^2-1\right].\left[32.(\frac{2}{9550}y-1)^6-48.(\frac{2}{9550}y-1)^4+18.(\frac{2}{9550}y-1)^2-1\right]+0.1 \quad (11)$$

$$f_4(x,y)=\frac{0.2}{\pi}\left[4.(\frac{2}{1400}x-1)^3-3.(\frac{2}{1400}x-1)\right].\left[8.(\frac{2}{9550}y-1)^4-8.(\frac{2}{9550}y-1)^2+1\right]+0.1 \quad (12)$$

$$f_5(x,y)=\frac{0.2}{\pi}\left[4.(\frac{2}{1400}x-1)^3-3.(\frac{2}{1400}x-1)\right].\left[16.(\frac{2}{9550}y-1)^5-20.(\frac{2}{9550}y-1)^3+5.(\frac{2}{9550}y-1)\right]+0.1 \quad (13)$$

$$f_6(x,y)=\frac{0.2}{\pi}\left[4.(\frac{2}{1400}x-1)^3-3.(\frac{2}{1400}x-1)\right].\left[32.(\frac{2}{9550}y-1)^6-48.(\frac{2}{9550}y-1)^4+18.(\frac{2}{9550}y-1)^2-1\right]+0.1 \quad (14)$$

Step 2: Structural strains $\varepsilon_1-\varepsilon_{30}$ at the locations of the strain gauges are simulated in ANSYS.

Step 3: The simulated local ice pressures $p_{31}-p_{36}$ at the locations of the local ice pressure gauges are obtained by Eq. (15), i.e., the equivalent uniform ice pressure within the induction board area was calculated:

$$p_i=\frac{1}{A}\iint_A f(x,y)dxdy \quad (15)$$

where

A is the induction board area of the local ice pressure gauge and

$f(x,y)$ is the load function.

Step 4: Addition of error $\{b\}'=\{b\}+\Delta\{b\}$; for the strain gauges used in the field test, the test error was set up as random data from -10 to 10 $\mu\varepsilon$; for the local ice pressure gauges, the test error was set up as random data from -3 to 3 kPa;

Step 5: The ice pressure distribution $\{f\}'$ is calculated using the HCM with the input of $\{b\}'$ obtained in Step 4.

Step 6: The equivalent uniform ice pressure within each individual cell is calculated by Eq. (16).

$$x_i = \frac{1}{a_i.b_i}\iint f(x,y)dxdy \tag{16}$$

where

a_i is the length of the individual cell No. i in X-direction, and

b_i is the length of the individual cell No. i in Y-direction.

Step 7: Comparing $\{f\}'$ with $\{f\}$.

The simulation results and error are shown in Fig. 13.

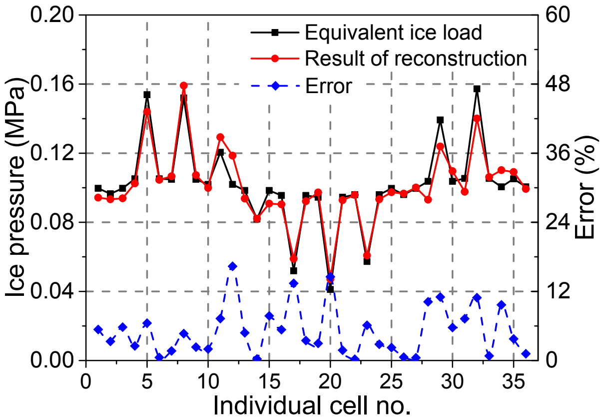

(a)

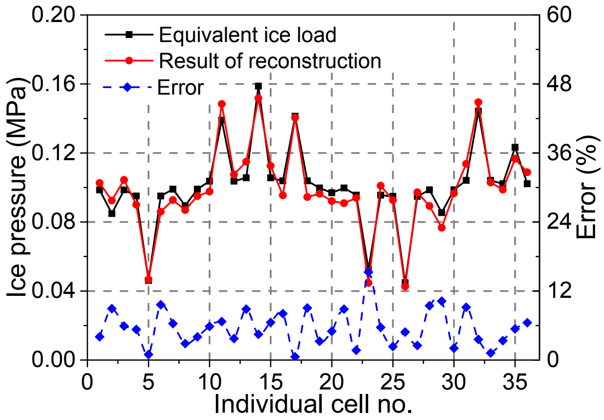

(b)

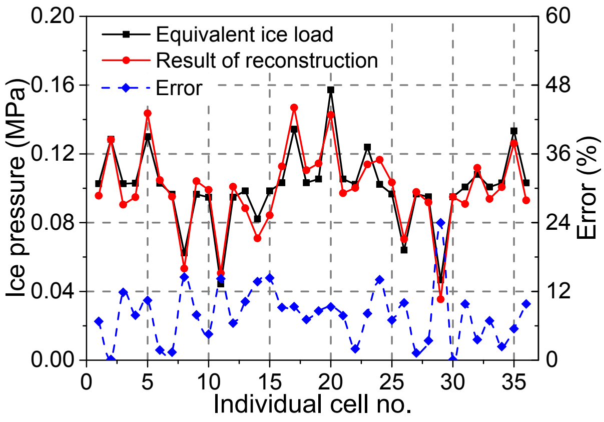

(c)

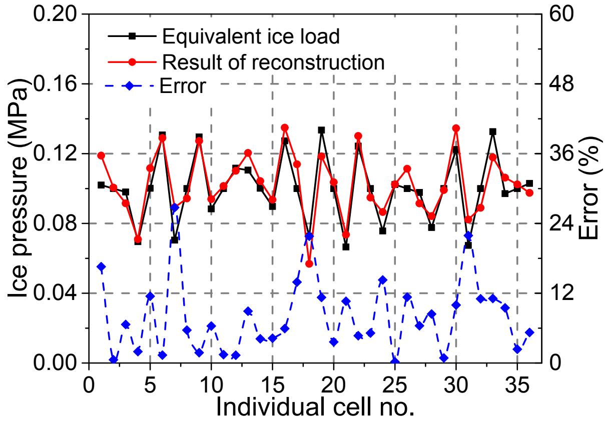

(d)

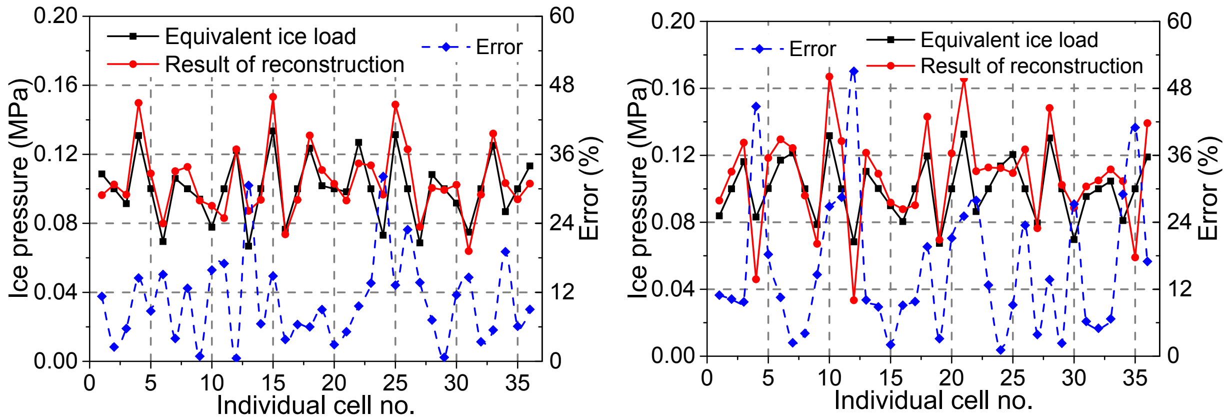

(e) (f)

Fig. 13 Simulation results for (a) $f_1(x,y)$ –(f) $f_6(x,y)$

Fig. 13 shows that the HCM produces accurate fittings for function-type loads $f_1(x,y)$ and $f_2(x,y)$. An obvious trend can be found from Fig. 13 that the accuracy of the ice load reconstruction drops gradually as the load function becomes more complex. Figs. 13(e) and 13(f) show that the accuracy of the ice load reconstruction can only be satisfactory for several individual cells, and the maximum error is larger than 50%. The correlation coefficients (CR) between the reconstructed ice pressure distribution $\{f\}'$ and the equivalent ice pressure distribution $\{f\}$ for $f_1(x,y)-f_6(x,y)$ were calculated and are shown in Fig. 14.

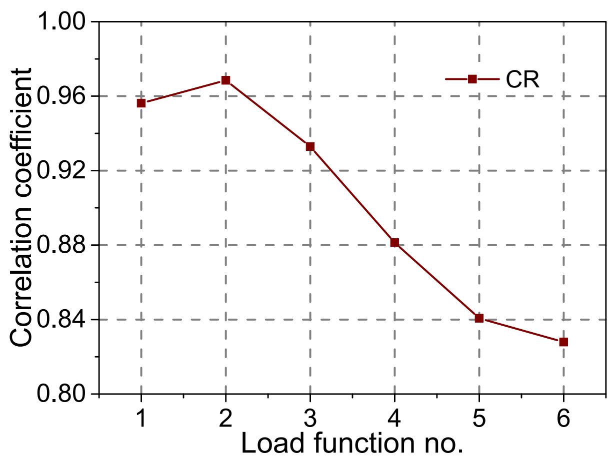

Fig. 14 Correlation coefficient between the reconstructed and the equivalent ice pressure distribution

It can be found from Fig. 14 that the CR between the equivalent ice pressure distribution of $f_2(x,y)$ and the reconstructed ice pressure distribution is the largest at approximately 0.969. In addition, the basic trend that the CR decreases as the load function becomes more complex is obvious. Thus, the assumption that the ice load is uniform within each individual cell with an area between 0.29 m^2 and 0.45 m^2 is only applicable to the situations where the load function is not complex.

The total ice forces of the function-type loads $f_1(x,y)-f_6(x,y)$ and the reconstructed ice loads were calculated and are shown in Fig. 15.

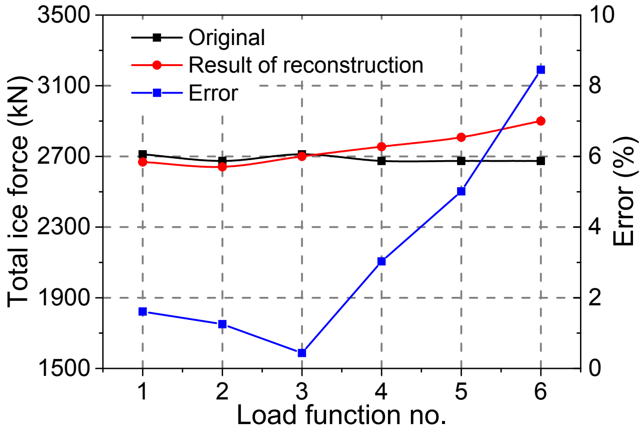

Fig. 15 Accuracy of total ice force

The maximum error of the total ice force is approximately 8.45%, as shown in Fig. 13, which means that the reconstruction result of the total ice force is more credible than that of the ice pressure distribution. Figs. 13–15 show approximately the same trend, in which the reconstruction accuracy of the ice pressure distribution and total ice force decreases gradually as the load functions become more complex.

5 Monitoring results

This section provides the actual measurements obtained from the sensors attached on the gate. The measured local ice pressure and strain corresponding to the lowest temperature of every day are shown in Figs. 16(a)–16(e), in which the temperature was measured by the thermistors fixed inside the strain and local ice pressure gauges. Actually, there are 30 temperature curves for the strain gauges, and as the difference between the 30 temperature curves is less than 2° C, the average temperature curve was used in Figs. 16(b)–16(e). Similarly, the average temperature curve of the local ice pressure gauges was used in Fig. 16(a). The measured water level is also shown in Fig. 16(f).

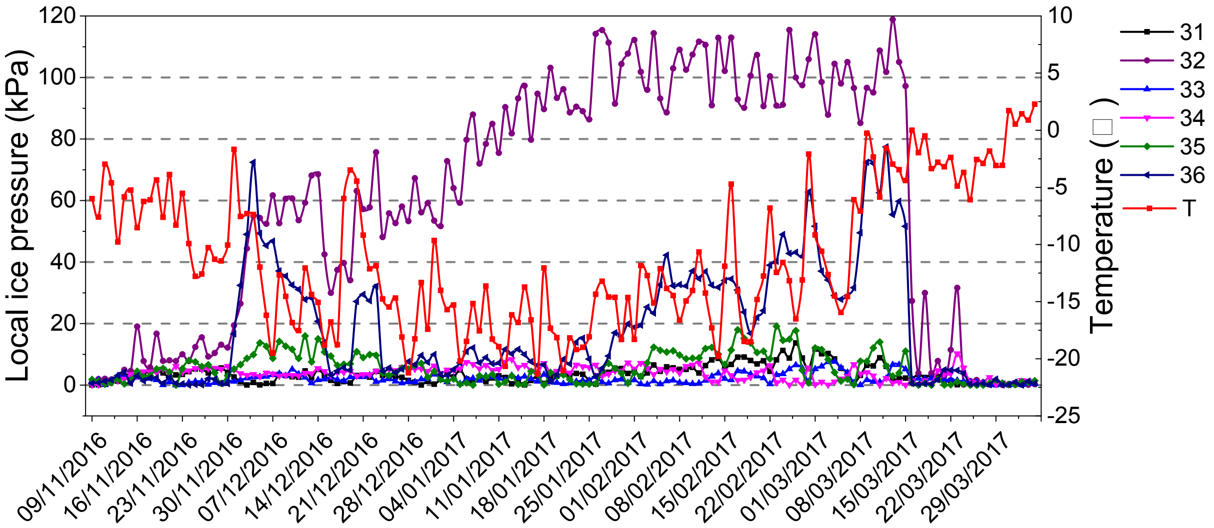

(a)

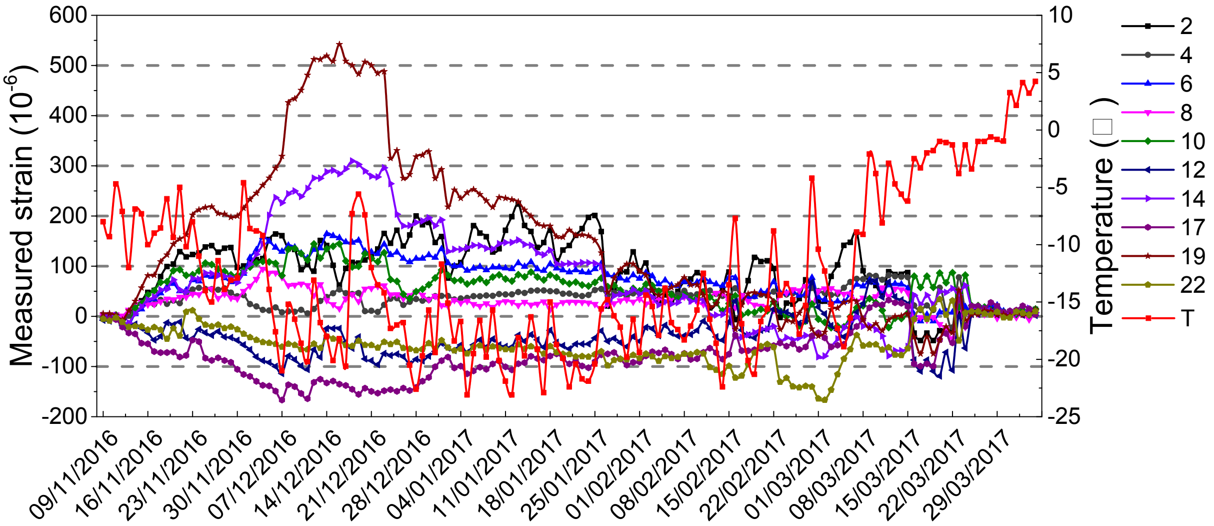

(b)

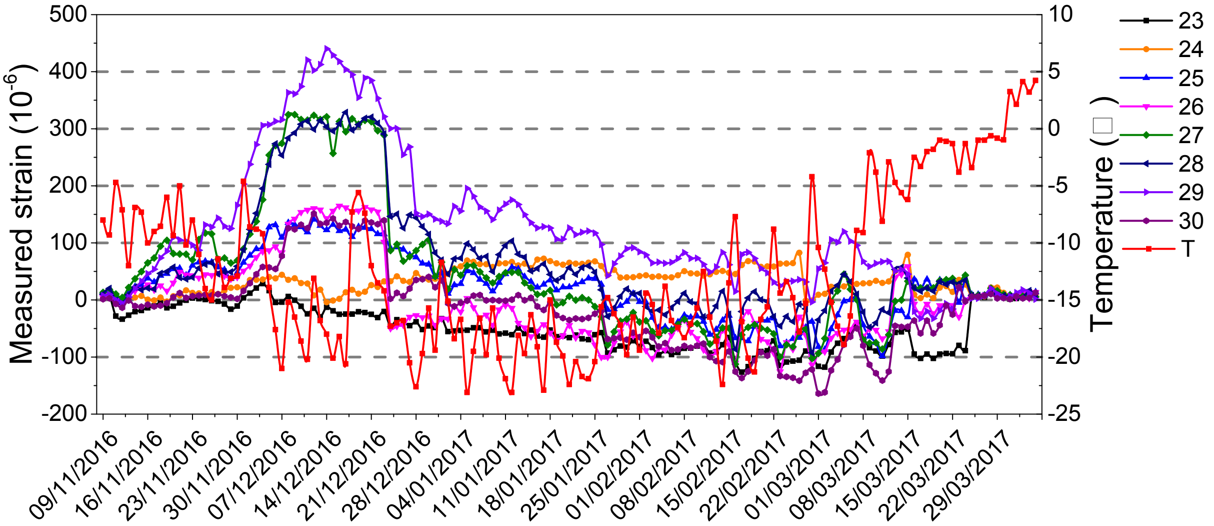
Measured strain (10^{-6})
Temperature (□)
23
24
25
26
27
28
29
30
T

(c)

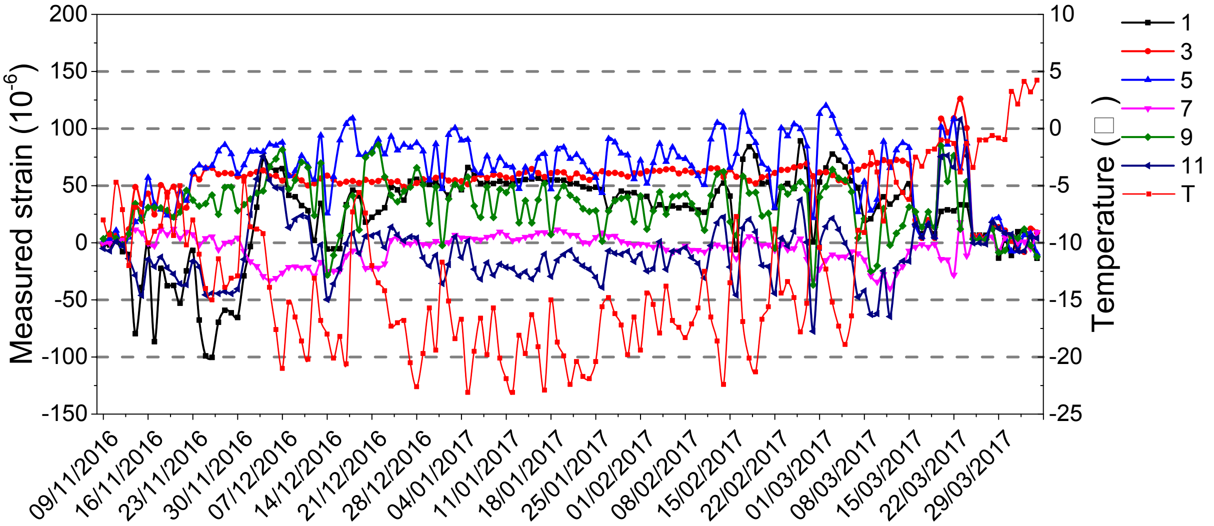
Measured strain (10^{-6})
Temperature (□)
1
3
5
7
9
11
T

(d)

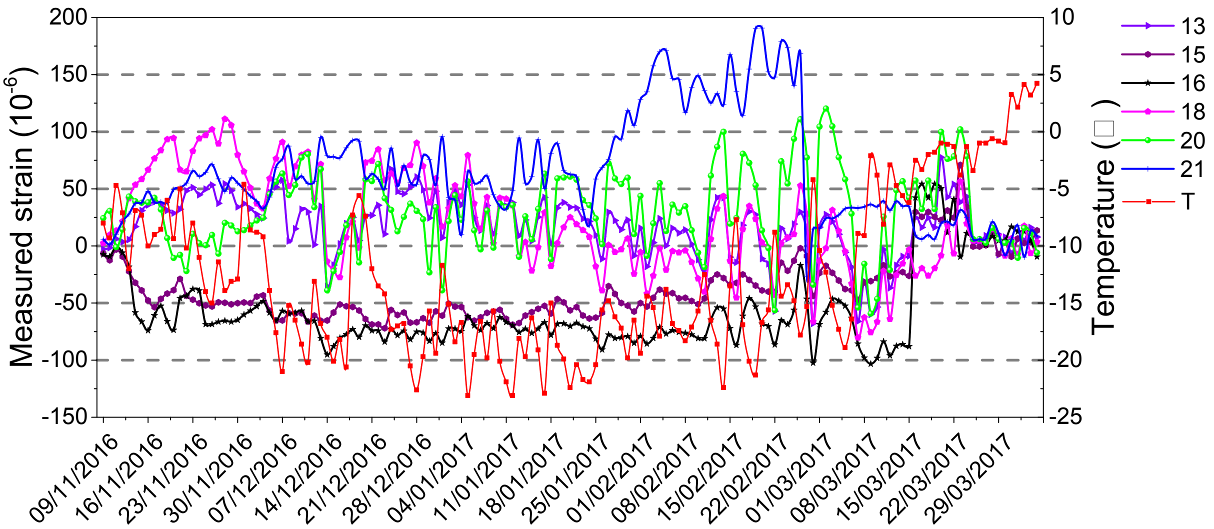
Measured strain (10^{-6})
Temperature (□)
13
15
16
18
20
21
T

(e)

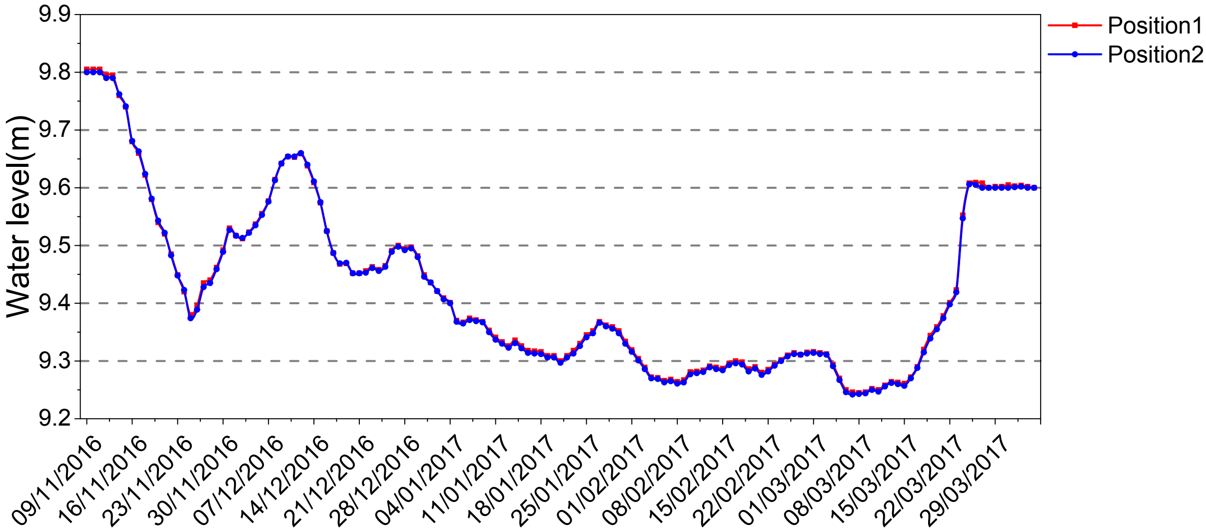

(f)

Fig. 16 Measured (a) local ice pressure, (b)–(c) vertical strain, (d)–(e) horizontal strain, and (f) water level corresponding to the lowest temperature in each day vs. the date

Fig. 16(f) shows that the maximum change in water level is approximately 0.55 m, which is very small, and can even be ignored.

6 Reconstruction of local ice pressure distribution

The monitoring data of strain and local ice pressure corresponding to the lowest temperature each day, as shown in Fig. 16(a)–Fig. 16(e), were chosen for the reconstruction of the ice pressure distribution through the HCM. The reconstruction results of the ice pressure distribution for 4 days are shown in Fig. 17.

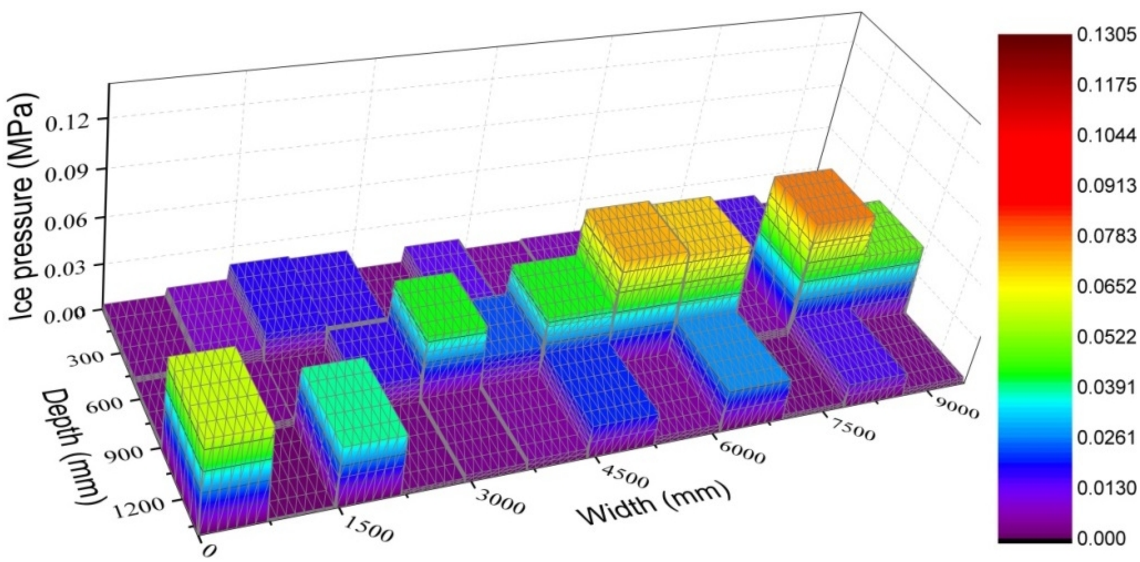

(a)

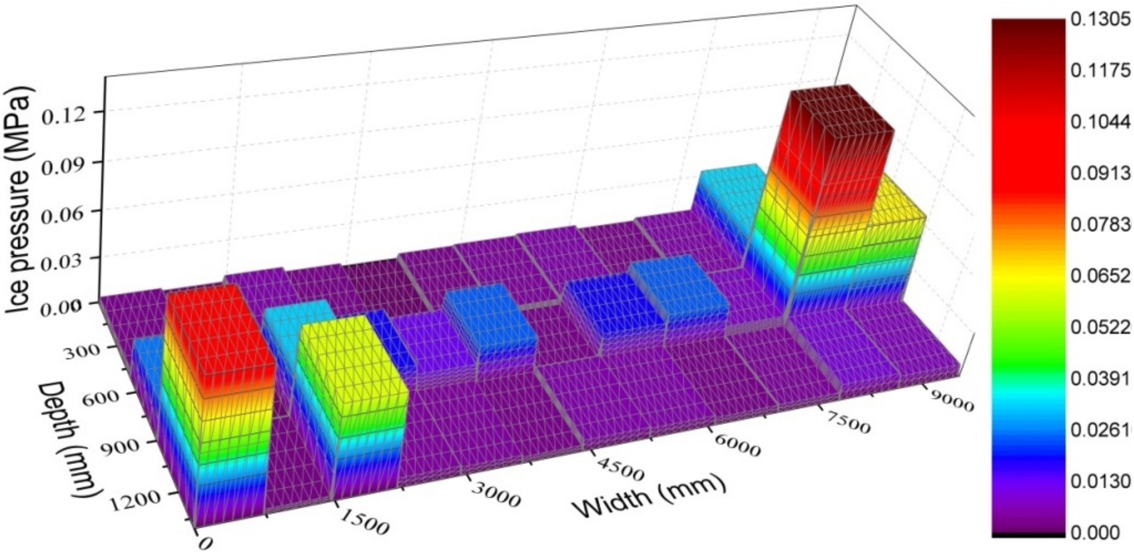

Ice pressure (MPa)
0.00
0.03
0.06
0.09
0.12
Depth (mm)
300
600
900
1200
Width (mm)
0
1500
3000
4500
6000
7500
9000
0.1305
0.1175
0.1044
0.0913
0.0783
0.0652
0.0522
0.0391
0.0261
0.0130
0.000

(b)

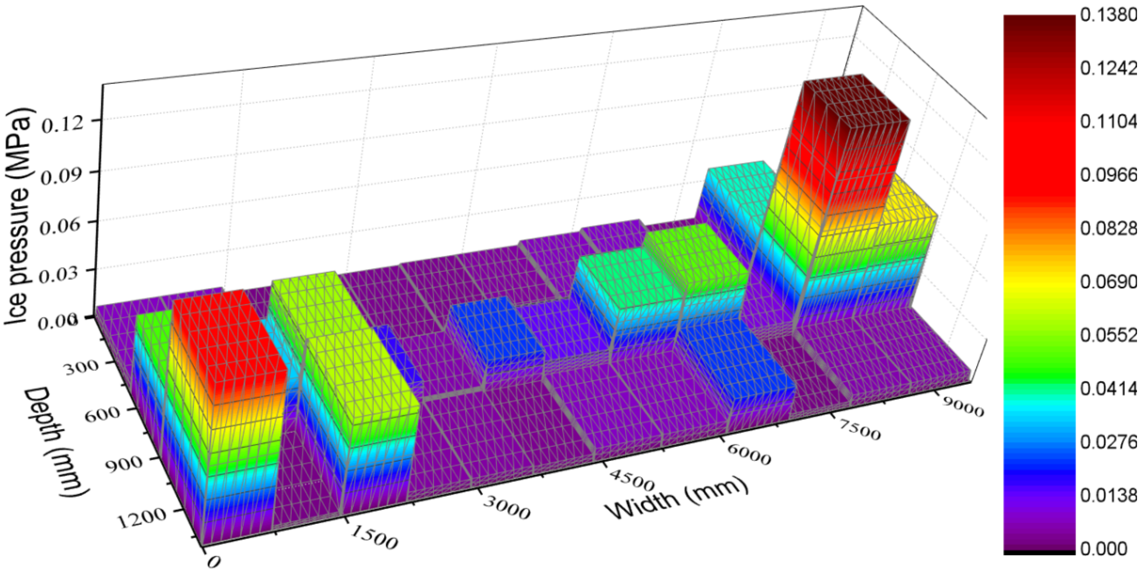

Ice pressure (MPa)
0.00
0.03
0.06
0.09
0.12
Depth (mm)
300
600
900
1200
Width (mm)
0
1500
3000
4500
6000
7500
9000
0.1380
0.1242
0.1104
0.0966
0.0828
0.0690
0.0552
0.0414
0.0276
0.0138
0.000

(c)

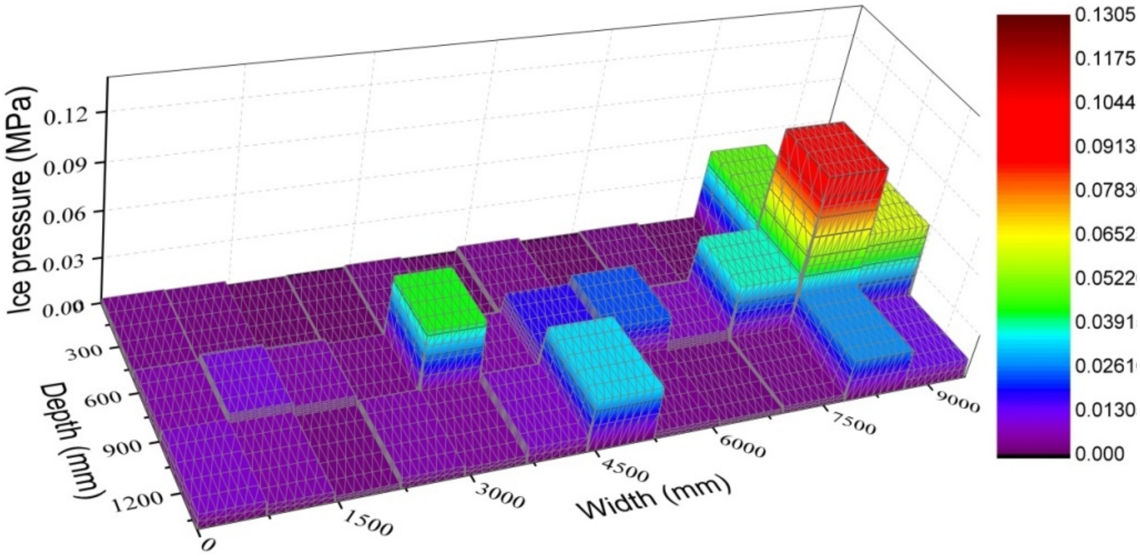

Ice pressure (MPa)
0.00
0.03
0.06
0.09
0.12
Depth (mm)
300
600
900
1200
Width (mm)
0
1500
3000
4500
6000
7500
9000
0.1305
0.1175
0.1044
0.0913
0.0783
0.0652
0.0522
0.0391
0.0261
0.0130
0.000

(d)

Fig. 17 Ice pressure distribution on (a) 20/12/2016, (b) 20/01/2017, (c) 20/02/2017, and (d) 20/03/2017, corresponding to the lowest temperature

Fig. 17 shows that the ice pressure distributions along the depth and width of the steel gate are not uniform, and all of the ice pressures are less than 0.14 MPa. The ice pressures on several individual cells are relatively large, such as those on the individual cells No. 3, No. 7, No. 9, No. 10, No. 14, No. 16, No. 20, No. 21, No. 23, No. 26, No. 27, No. 31, No. 32, and No. 35. It can be found from the monitoring data of local ice pressures, as shown in Fig. 16(a), that the ice pressure is not uniform along the depth and width of the gate, which is consistent with the reconstruction results of ice pressure, as shown in Fig. 17.

The ice pressures within those individual cells throughout the monitoring period were reconstructed and are shown in Fig. 18.

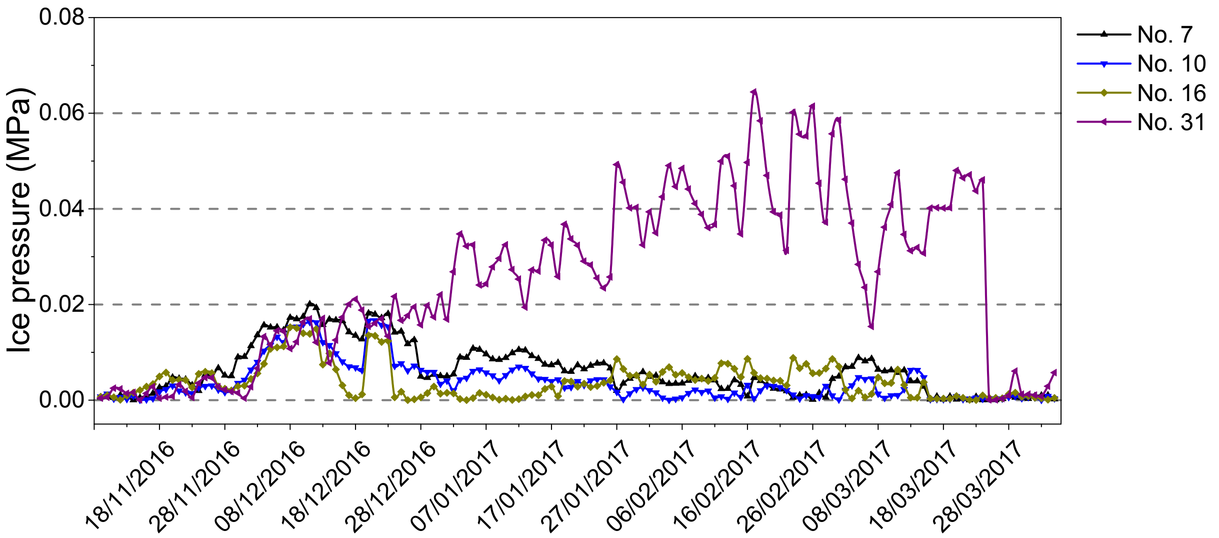

(a)

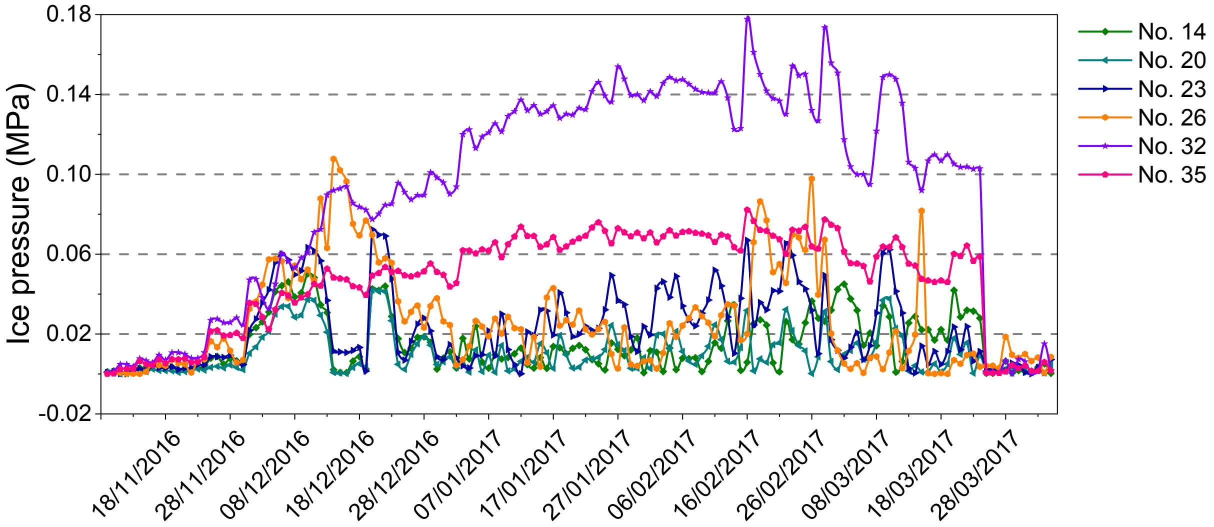

(b)

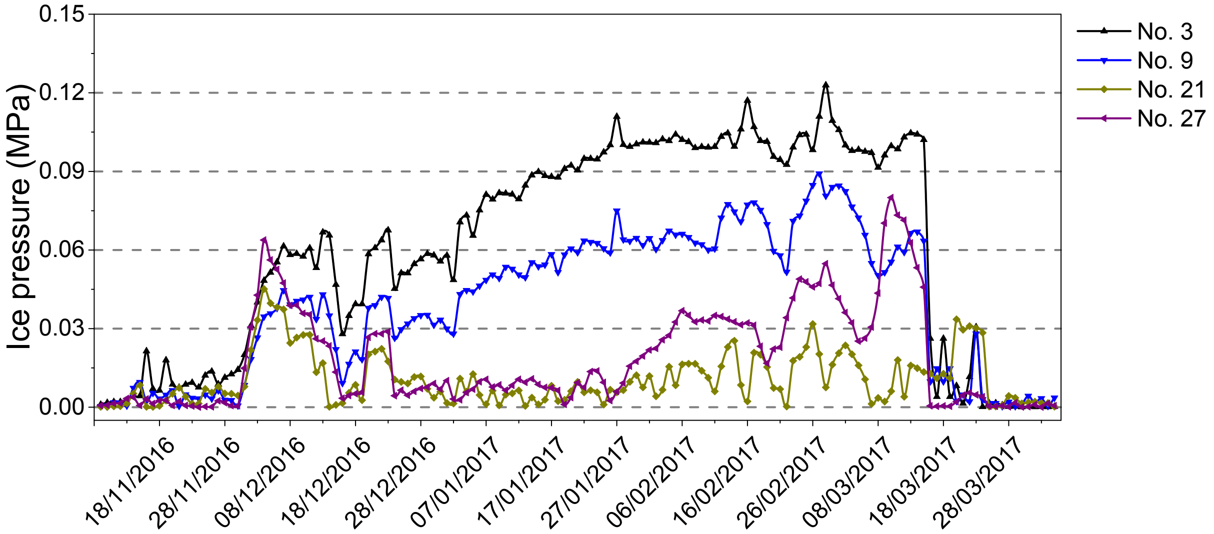

(c)

Fig. 18 Ice pressure within several individual cells for (a) upper individual cells, (b) middle individual cells, and (d) lower individual cells

Fig. 18 shows that only the ice pressures within the individual cells No. 3, No. 9, No. 26 No. 27, No. 31, No. 32, and No. 35 exceeded 0.06 MPa during some periods.

The Songhua River began to freeze at the end of October 2016, and a complete ice layer was formed by approximately November 7th. The thickness of the ice layer was approximately 22 cm in the river centre, 33 cm at ten metres in front of the gate, and 92 cm at one metre in front of the gate on November 30th. The back side of the gate was directly exposed to the cold air, and the upper surface of the ice layer had indirect contact with the cold air because of the snow cover.

These factors, together with the excellent thermal conductivity of steel, resulted in the larger thickness of the ice layer near the gate, which is in line with the in-situ observations of a vertical steel core in a cold region (Sharapov et al., 2014). Thus, the ice layer reached the lower individual cells on November 30th.

Fig. 18 shows that the ice pressures began to increase from the beginning of December. The ice pressures of most individual cells began to decrease from approximately December 12th, which very likely was caused by the partial debonding of the ice layer from the steel gate, as shown in Fig. 19. Then, several days later, the ice pressures recovered their growth.

Fig. 19 Partial debonding of the ice layer and gate

Fig. 16(f) shows that the water level began to decrease slowly from December 13th. Although Comfort and Abdelnour (1992) believed that a decrease in the water level can result in tension in the upper part and compressive stress in the lower part of the ice layer near a dam, the effect of a slow decrease in the water level on the ice pressure distribution of the gate was not obvious, as shown in Fig. 18.

Once the ice pressure distributions throughout the entire monitoring period were reconstructed, the average ice line load can be calculated by Eq. (17).

$$F = \frac{\sum_{i=1}^{36} A_i . f_i}{L/2} \tag{17}$$

where

F is the average ice line load ($kN.m^{-1}$),

A_i is the area of the individual cell No. i (mm^2),

f_i is the equivalent uniform ice pressure of the individual cell No. i (MPa), and

L is the width of the steel gate (mm).

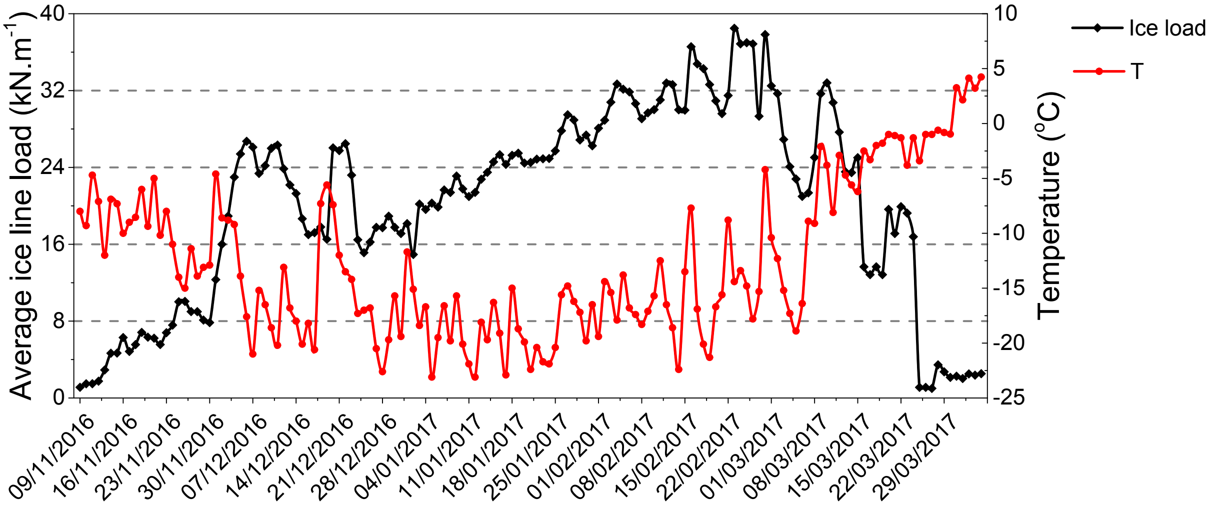

Fig. 20 Average ice line load

Fig. 20 shows that the average ice line load increased quickly during the early days of the freezing period, and then the average ice line load decreased from approximately December 12th, which was very likely due to the partial debonding of the ice from the gate, as shown in Fig. 19. Subsequently, the average ice line load increased nearly linearly with some fluctuations from 25/12/2016 to 28/02/2017, during which the average ice line load reached the maximum of 38 $kN.m^{-1}$ on 23/02/2017.

The structural strain of the steel gate was monitored, and the ice pressure distribution was identified with the M-P inverse method by Zhang et al. (2018), in which the ice loading zone of the gate was divided into 10 individual cells. The areas of the individual cells were 1.87 m^2 and

1.25 m^2, which were too large for identifying the ice pressure distribution accurately. However, the accuracy of the average ice line load was likely to be higher than that of the ice pressure distribution. Additionally, stress metres were arranged on the stoplogs to measure the ice stress, from which the average ice line load exerted on the stoplogs can be determined (Gong et al., 1999). The steel gate and steel stoplogs were similar in material, function, and structure, and the average ice thickness in front of the steel gate and steel stoplogs was almost the same. Therefore, the average ice line loads provided by Zhang et al. (2018) and Gong et al. (1999) were used for the comparison. The average ice line load during the middle and late period of the 1996–1997 and 1997–1998 winters were provided by Gong et al. (1999), which were calculated with the monitoring data from the stress meters. Thus, the four sets of results during the middle and late period of the winter were compared, as shown in Fig. 21.

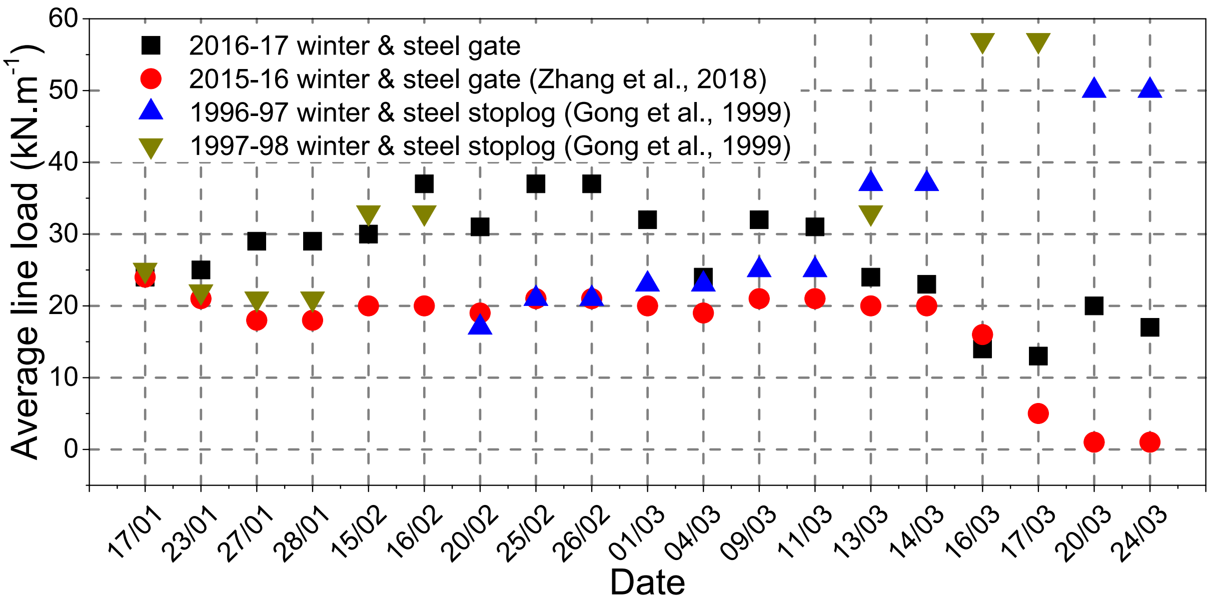

Fig. 21 Comparison of four average ice line loads

It can be found from Fig. 21 that the average ice line load of the steel gate during the winter of 2015–2016 was close to that of the stoplogs during the winters of 1996–1997 and 1997–1998 before March 11. Overall, the average ice line load of the steel gate during the winter of 2016–

2017 was the largest before March 11. After March 11, the average ice line load of the steel gate gradually decreased. In contrast, the average ice line load of the stoplogs increased.

Although the monitoring data and the method used to reconstruct the ice pressure distribution are different from those in the research of Zhang et al. (2018), the monitored steel gate is the same. Therefore, the average ice line loads corresponding to the lowest temperature of each day during the two monitoring periods were directly compared, as shown in Fig. 22.

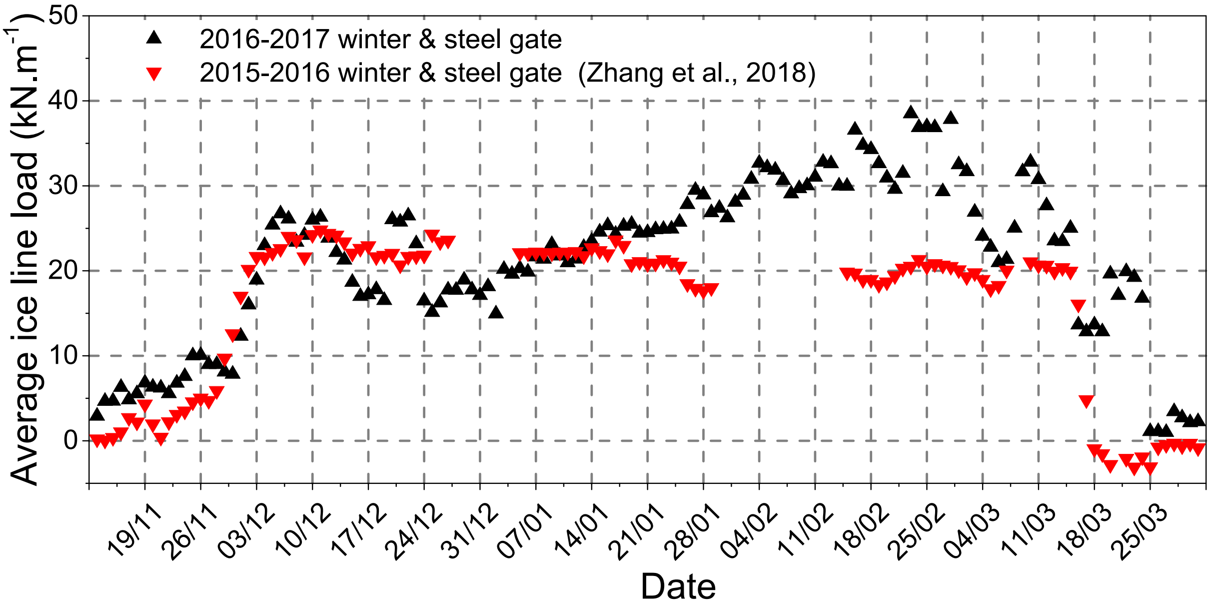

Fig. 22 Comparison of various research results

It can be found from Fig. 22 that the average ice line load is similar to the results of Zhang et al. (2018) from the beginning of the winter to approximately January 20th, and the difference between the two average ice line loads began to gradually increase from January 20th. The average ice line load reached the maximum value of 38 $kN.m^{-1}$ on 23/02/2017, while the average ice line load provided by Zhang et al. (2018) reached the maximum value of 25 $kN.m^{-1}$ on 11/12/2015. Additionally, the rapid decrease in the average ice line load occurred later, compared with the average ice line load decrease provided by Zhang et al. (2018).

7 Conclusions

In this study, the structural strain and local ice pressure of a steel gate were monitored by 30 strain gauges and 6 ice pressure gauges during the winter of 2016–2017. The pre-estimated ice loading area was divided into 72 individual cells, which are symmetrical about the centre line of the gate, and mathematical models for the reconstruction of ice pressure distribution were established based on the assumption that the ice pressure was equivalent and uniform within each individual cell.

The HCM was developed for solving the mathematical models and reconstructing the approximate ice pressure distribution on the gate, using the data collected by the strain and local ice pressure gauges. The approximate ice pressure distribution was then reconstructed, and the average ice line load was calculated. The maximum ice pressure was approximately 0.18 MPa on 16/02/2017. The maximum line load was 38 kN.m^{-1} on 23/02/2017.

However, there are limitations to this study, such as there is no criterion to judge whether the size of an individual cell is suitable for the reconstruction of the ice pressure distribution. Therefore, the criterion mentioned above should be one of the research priorities in the future.

Acknowledgements

This work was sponsored and supported by the Science and Technology Project of Western Transportation Construction, Ministry of Transport of the People's Republic of China (2014364554050). The work was also supported by the National Key Research and Development Plan, Ministry of Science and Technology of the People's Republic of China (2018YFC0310500).

References

Badran, S.F., Nassef, A.O. and Metwalli, S.M., 2009. Y-stiffened panel multi-objective optimization using genetic algorithm. Thin-Walled Structures, 47(11): 1331-1342.

Brown, T.G., 2007. Analysis of ice event loads derived from structural response. Cold Regions Science & Technology, 47(3): 224-232.

Brown, T.G., Tibbo, J.S., Tripathi, D., Obert, K. and Shrestha, N., 2010. Extreme ice load events on the Confederation Bridge. Cold Regions Science & Technology, 60(1): 1-14.

Chai, W., Leira, B.J. and Naess, A., 2018. Probabilistic methods for estimation of the extreme value statistics of ship ice loads. Cold Regions Science and Technology, 146: 87-97.

Chuang, Y.-C., Chen, C.-T. and Hwang, C., 2016. A simple and efficient real-coded genetic algorithm for constrained optimization. Applied Soft Computing, 38: 87-105.

Coates, C.W. and Thamburaj, P., 2008. Inverse Method Using Finite Strain Measurements to Determine Flight Load Distribution Functions. Journal of Aircraft, 45(2): 366-370.

Comfort, G., Gong, Y., Singh, S. and Abdelnour, R., 2003. Static ice loads on dams. Canadian Journal of Civil Engineering, 30(1): 42-68.

Comfort, G. and Abdelnour, R., 1992. Field measurements of ice pressures on the Paugan Dam. Proc., CDSA-CANCOLD conf., Quebec City, Quebec, pp. 1-19.

Comfort, G., Liddiard, A. and Abdelnour, R., 2004. A method and tool for predicting static ice loads on dams. 17th Int. Symp. on Ice, pp. 96-104.

Deep, K., Singh, K.P., Kansal, M.L. and Mohan, C., 2009. A real coded genetic algorithm for solving integer and mixed integer optimization problems. Applied Mathematics & Computation, 212(2): 505-518.

Ewins D.J., 2000, Modal Testing: Theory, Practice and Application. Wiley.

Gagnon, R., 2008. Analysis of data from bergy bit impacts using a novel hull-mounted external Impact Panel. Cold Regions Science & Technology, 52(1): 50-66.

Gong, Y., Penner, R., Comfort, G., Armstrong, T., 1999. Static Ice Loads on Wooden and Steel Stoplogs at Seven Sisters Generating Station. Proceedings, 10th Workshop on River Ice Winnipeg, Manitoba, Canada, pp. 70-84.

Hansen, P.C., 2007. Regularization Tools version 4.0 for Matlab 7.3. Numerical Algorithms, 46(2): 189-194.

Jeon, M., Choi, K., Min, J.K. and Ha, J.S., 2018. Estimation of local ice load by analyzing shear strain data from the IBRV ARAON's 2016 Arctic voyage. International Journal of Naval Architecture & Ocean Engineering.

Johnston, Timco, G.W, Frederking and Miles, 2008. Measuring global impact forces on the CCGS Terry Fox with an inertial measurement system called MOTAN. Cold Regions Science & Technology, 52(1): 67-82.

Kalhori, H., Ye, L., Mustapha, S., Li, J. and Li, B., 2016. Reconstruction and Analysis of Impact Forces on a Steel-Beam-Reinforced Concrete Deck. Experimental Mechanics, 56(9): 1-12.

Kharik, E., Roubtsova, V., Morse, B., 2015. Impact of ice type on predicted ice load for dams. 18th Workshop on the Hydraulics of Ice Covered Rivers, Quebec City, QC, Canada.

Kim, H., Daley, C. and Colbourne, B., 2018. A study on the evaluation of ice loads and pressure distribution using Pressure Indicating Film in ice-structure interaction. Ocean Engineering, 165: 77-90.

Kjerstad, Ø.K., Lu, W., Skjetne, R. and Løset, S., 2018. A method for real-time estimation of full-scale global ice loads on floating structures. Cold Regions Science and Technology.

Lee, J.M., Lee, C.J., Kim, Y.S., Choi, G.G. and Lew, J.M., 2016. Determination of global ice loads on the ship using the measured full-scale motion data. International Journal of Naval Architecture & Ocean Engineering, 8(4): 301-311.

Lee, T.K., Lee, J.H., Kim, H. and Rim, C.W., 2014. Field measurement of local ice pressures on the ARAON in the Beaufort Sea. International Journal of Naval Architecture & Ocean Engineering, 6(4): 788-799.

Lourens, E. and Fallais, D.J.M., 2017. On the use of equivalent forces for structural health monitoring based on joint input-state estimation algorithms. Procedia Engineering, 199: 2140-2145.

Maes, K., Nimmen, K.V., Lourens, E., Rezayat, A., Guillaume, P., Roeck, G.D. and Lombaert, G., 2016. Verification of joint input-state estimation for force identification by means of in situ measurements on a footbridge. Mechanical Systems and Signal Processing, 75: 245-260.

Nakamura, T., Igawa, H. and Kanda, A., 2012. Inverse identification of continuously distributed loads using strain data. Aerospace Science & Technology, 23(1): 75-84.

Ritch, R., Frederking, R., Johnston, M., Browne, R. and Ralph, F., 2008. Local ice pressures measured on a strain gauge panel during the CCGS Terry Fox bergy bit impact study. Cold Regions Science & Technology, 52(1): 29-49.

Sang, C.L., Park, S., Choi, K. and Jeong, S.Y., 2018. Prediction of ice loads on Korean IBRV ARAON with 6-DOF inertial measurement system during trials of Chukchi and East Siberian Seas. Ocean Engineering, 151: 23-32.

Sharapov, D. and Shkhinek, K., 2014. A method to determine the horizontal ice loads on the vertical steel structures which adfreeze to the ice level. Coastal Engineering, 88(88): 69-74.

Stander, E., 2006. Ice Stresses in Reservoirs: Effect of Water Level Fluctuations. Journal of Cold Regions Engineering, 20(2): 52-67.

Taras, A., Côté, A., Comfort, G., Thériault, L., Morse, B., 2011. Measurements of Ice thrust at Arnprior and Barrett Chute Dams. 16th CRIPE Workshop, pp. 317-328.

The Ministry of Water Resources of People's Republic of China, 2013. Design code for steel gate in water resources and hydropower projects (SL74).

Tsoulos, I.G., 2008. Modifications of real code genetic algorithm for global optimization. Applied Mathematics & Computation, 203(2): 598-607.

Tutkun, N., 2009. Parameter estimation in mathematical models using the real coded genetic algorithms. Expert Systems with Applications, 36(2): 3342-3345.

Wang, L., Cao, H. and Xie, Y., 2015. An Improved Iterative Tikhonov Regularization Method for Solving the Dynamic Load Identification Problem. International Journal for Computational Methods in Engineering Science & Mechanics, 16(5): 292-300.

Xu, N. and Yue, Q., 2010. Dynamic Ice Forces Analysis of Conical Structure Based on Direct Measurement, ASME 2010 International Conference on Ocean, Offshore and Arctic Engineering, pp. 771-776.

Yue, Q. and Bi, X., 2000. Ice-Induced Jacket Structure Vibrations in Bohai Sea. Journal of Cold Regions Engineering, 14(2): 81-92.

Zhang, M., Qu, X., Kalhori, H. and Ye, L., 2018. Indirect monitoring of distributed ice loads on a steel gate in a cold region. Cold Regions Science & Technology, 151: 267-287.